Cui *et al. Energy Mater* 2024;4:400057
DOI: 10.20517/energymater.2023.134

Energy Materials

Review

Open Access

Check for updates

Emerging MXene-based electrocatalysts for efficient nitrate reduction to ammonia: recent advance, challenges, and prospects

Zhijie Cui[1], Chunli Li[1,*], Wenchao Peng[2], Jiapeng Liu[1,*]

[1]School of Chemical Engineering and Technology, National-Local Joint Engineering Laboratory for Energy Conservation in Chemical Process Integration and Resources Utilization, Tianjin Key Laboratory of Chemical Process Safety, Hebei University of Technology, Tianjin 300130, China.
[2]School of Chemical Engineering and Technology, Tianjin University, Tianjin 300072, China.

***Correspondence to:** Prof. Chunli Li, School of Chemical Engineering and Technology, National-Local Joint Engineering Laboratory for Energy Conservation in Chemical Process Integration and Resources Utilization, Hebei University of Technology, Xiping Road 5340, Tianjin 300130, China. E-mail: lichunli_hebut@126.com; Prof. Jiapeng Liu, School of Chemical Engineering and Technology, National-Local Joint Engineering Laboratory for Energy Conservation in Chemical Process Integration and Resources Utilization, Hebei University of Technology, Xiping Road 5340, Tianjin 300130, China. E-mail: liujiapeng@hebut.edu.cn

How to cite this article: Cui Z, Li C, Peng W, Liu J. Emerging MXene-based electrocatalysts for efficient nitrate reduction to ammonia: recent advance, challenges, and prospects. *Energy Mater* 2024;4:400057. https://dx.doi.org/10.20517/energymater.2023.134

Received: 30 Dec 2023 **First Decision:** 8 Apr 2024 **Revised:** 25 Apr 2024 **Accepted:** 30 May 2024 **Published:** 4 Jun 2024

Academic Editors: Wei Tang, Hao Liu **Copy Editor:** Fangyuan Liu **Production Editor:** Fangyuan Liu

Abstract

Ammonia (NH_3) plays an irreplaceable role in traditional agriculture and emerging renewable energy. Its preparation in industry mainly relies on the energy-intensive Haber-Bosch process, which is associated with high energy consumption and large CO_2 emissions. Recently, the nitrate reduction reaction (NO_3^-RR) driven by renewable energy has received extensive attention. This reaction can efficiently synthesize NH_3 with water as a hydrogen source and NO_3^- as a nitrogen source under mild conditions, which is conducive to reducing energy consumption and promoting the carbon cycle. It is well known that the properties of electrocatalysts determine the performance of NO_3^-RR. As an emerging two-dimensional material, MXenes (transition metal carbides/nitrides/carbon nitrides) possess excellent electrical conductivity, large specific surface area and controllable surface functional groups, which shows great application potential in the field of NO_3^-RR. Herein, this review summarized the structure, properties and synthesis strategies of MXenes to elucidate the possibilities from foundation to application. Then, the latest research progress in applying MXene-based electrocatalysts to NO_3^-RR was summarized and the applicability of different NH_3 detection methods was analyzed. Finally, the present challenges and future prospects of NO_3^-RR were presented. This review aimed to provide thoughtful insights into the rational design of MXene-based electrocatalysts for sustainable NH_3 synthesis.

Keywords: Nitrate reduction reaction, MXenes, electrocatalysis, ammonia synthesis

INTRODUCTION

Ammonia (NH_3) plays an irreplaceable role in many fields of modern society[1]. In the agricultural sector, NH_3 is one of the important raw materials for manufacturing fertilizer[2]. In the field of energy, liquid NH_3 has become a promising hydrogen carrier due to its mature transportation network, high volume energy density (12.7 MJ L^{-1}), and mass hydrogen content (17.6 wt%)[3]. With the development of industry, the demand for NH_3 is increasing. Large-scale synthesis of NH_3 relies on the industrial Haber-Bosch process (HBP), which reacts N_2 and H_2 to synthesize NH_3 at high temperatures (400-600 °C) and pressures (20-40 MPa)[4,5]. However, it consumes 1%-2% of the global energy each year and accounts for 1.2% of global CO_2 emissions[6]. Therefore, it is of great significance to develop an environmentally friendly and low-energy technology for the sustainable NH_3 synthesis.

NH_3 synthesis via nitrogen reduction reaction (NRR) has received extensive attention and research in the past decade[7,8]. However, the extremely high dissociation energy of N≡N bond (942 kJ mol^{-1}) and low solubility in water (0.024) severely limit the performance of NRR[9,10]. Recently, emerging environmentally friendly technologies have received wide attention, such as microbial electrochemistry technologies, nitrate reduction reaction (NO_3^-RR), and so on[11]. Compared to NRR, NO_3^-RR uses NO_3^- in wastewater as a nitrogen source. On the one hand, the relatively friendly N=O dissociation energy (204 kJ mol^{-1}) and the high solubility accelerate the reaction kinetics of NO_3^-RR[12]. On the other hand, due to the unreasonable discharge of industrial wastewater, NO_3^- has become one of the most widespread groundwater pollutants in the world. However, NO_3^-RR involves a complex process of protons coupling electrons, inevitably leading to high overpotential, slow reaction kinetics, and low selectivity (such as N_2, N_2O, NO, NO_2, N_2H_4 and NH_2OH). In addition, the competition of hydrogen evolution reaction (HER) is also the main reason that affects the Faradaic efficiency (FE) of NO_3^-RR[13]. As the core of the electrocatalytic system, the electrocatalyst performance directly determines the efficiency, reliability and economy of NH_3 synthesis[14,15]. Therefore, developing efficient and stable electrocatalysts is key to the advancement of NO_3^-RR. Since the discovery of single-layer graphene, researchers have set off an upsurge of research on two-dimensional (2D) materials. Recently, as a new class of 2D nanomaterials, transition metal carbides/nitrides/carbon nitrides (MXenes) have been extensively studied due to their high electrical conductivity, adjustable surface functional groups and large specific surface area[16,17]. Since Naguib *et al.* discovered the first MXenes material (Ti_3C_2) in 2011, more than 40 MXenes have been synthesized and widely used in electrocatalysis[18]. In particular, the inherent outstanding properties of MXenes make them show great potential in the application of NO_3^-RR [Figure 1A].

Up to now, there has been no review of MXene-based materials for electrocatalytic NO_3^- reduction to NH_3. Herein, this review summarized the structure, properties and synthesis strategies of MXenes to elucidate the possibilities from foundation to application. Then, the latest advance of MXene-based electrocatalysts for NO_3^-RR was elaborated, and the applicability of different NH_3 detection methods was analyzed. Finally, NO_3^-RR was expected from catalyst design, reaction mechanism, comprehensive energy utilization and industrialization [Figure 1B].

STRUCTURE, PROPERTIES AND SYNTHESIS STRATEGIES OF MXENES

As a new class of the 2D material family, MXenes show great potential in NO_3^-RR. Their inherent properties play an important role in the catalytic activity of NO_3^-RR. Therefore, the following chapters summarize their structure, properties and synthesis strategies in detail, which is conducive to a deeper understanding of MXenes and their applications.

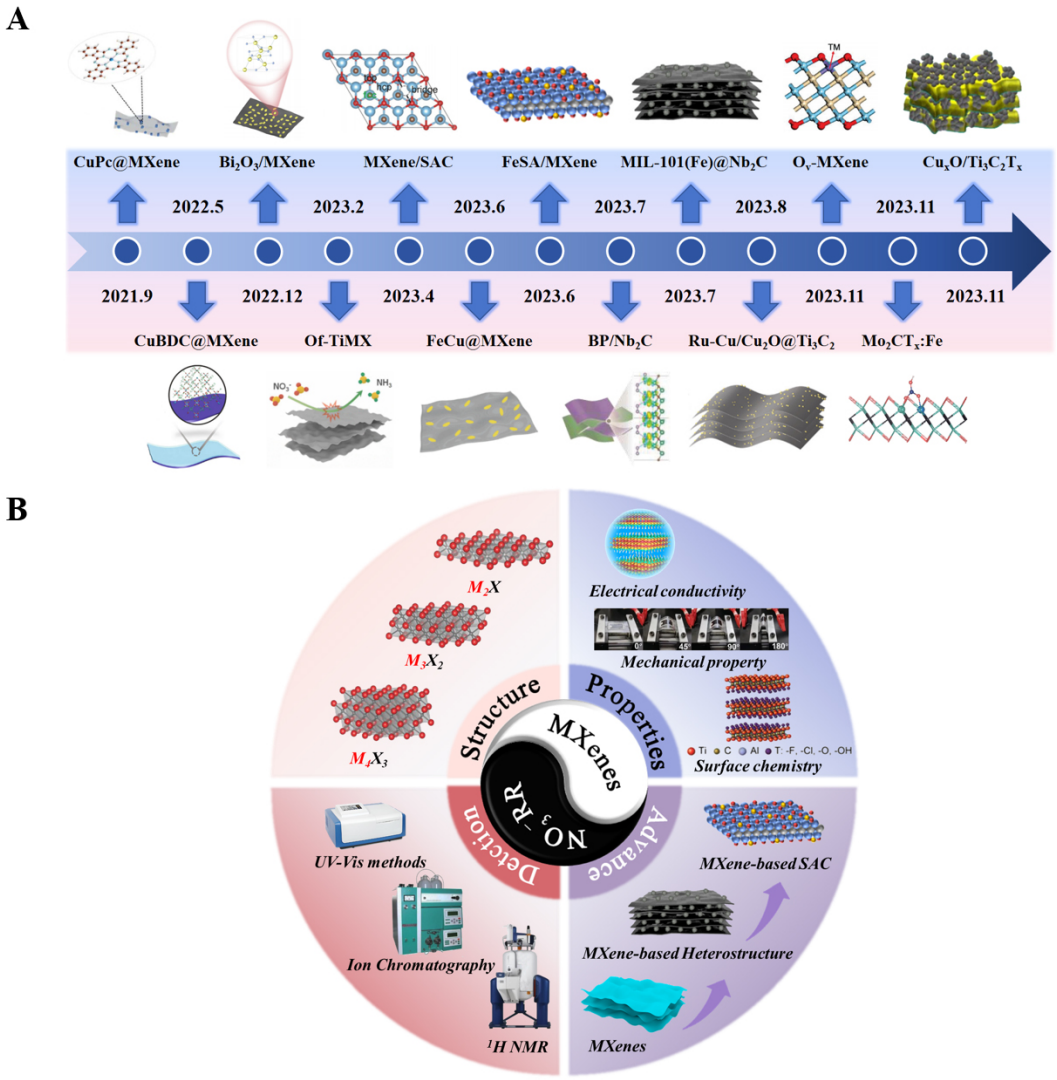

Figure 1. (A) Summary of the MXene-based electrocatalysts for NO_3^-RR. (B) A simple timeline summarizes the latest advances in MXene-based electrocatalysts.

Structure of MXenes

Naguib *et al.* at Drexel University found that the Al atoms in Ti_3AlC_2 MAX can be selectively etched by HF to obtain a $Ti_3C_2T_x$ MXene with rich surface functional groups[18]. In the following studies, a class of 2D transition metal carbon/nitrogen/carbonitrogen compounds (MXenes) can be derived by selective etching of the A atom in the MAX phase (the molecular formula is $M_{n+1}AX_n$, where A is the main group elements from I B to VI A)[19]. The molecular formula of MXenes is $M_{n+1}X_nT_x$, where M is mainly a pre-transition metal (Sc, Ti, V, Cr, Mn, Zr, Nb, Mo, Hf, Ta), X is C, N, or CN, T_x is the surface end group (-O, -OH, -F, *etc.*), and *n* ranges from 1 to 4 [Figure 2A][20]. In the structure of MXenes, the atoms of the X element occupy octahedral interstitial sites of M in their hexagonal crystal sublattices, which results in sharing the subunits of the edge M_6X octahedron[21].

The layered structure of MXenes can be clearly observed by scanning electron microscopy (SEM) [Figure 2B][22]. After further ultrasonic or intercalation treatment, MXene nanosheets with few or single

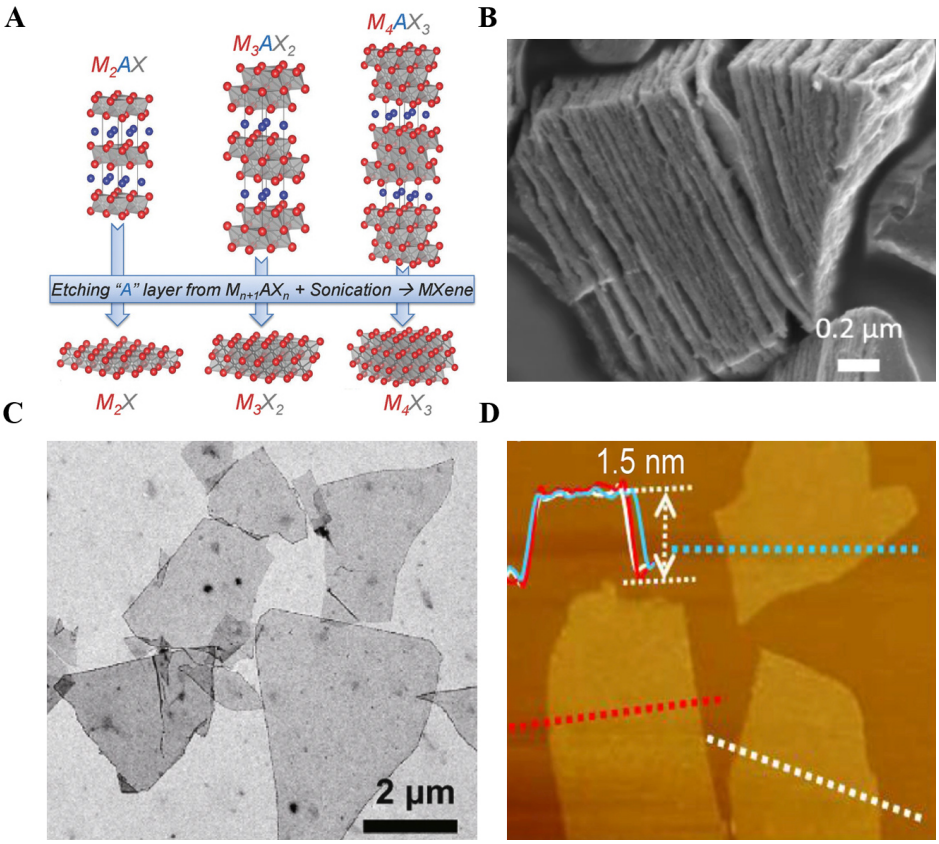

Figure 2. (A) Schematic diagram of MXene species. Reproduced with permission from Ref.[20]. Copyright 2014 Wiley-VCH. (B) SEM image of multi-layer MXene. Reproduced with permission from Ref.[22]. Copyright 2021 Springer Nature. (C) TEM image of MXene with few or single layers. Reproduced with permission from Ref.[23]. Copyright 2021 Springer Nature. (D) AFM image of single-layer MXene. Reproduced with permission from Ref.[24]. Copyright 2019 Elsevier.

layers can be obtained. As shown in transmission electron microscopy (TEM), MXenes can be intuitively seen to have the characteristics of ultra-thin nanosheets [Figure 2C][23]. The thickness of the MXene nanosheets with monolayers can be accurately measured by atomic force microscopy (AFM) with a thickness of about 1 nm, further demonstrating its atomically thin properties [Figure 2D][24].

Properties of MXenes

As a material with a unique 2D layered structure, MXenes exhibit high electrical conductivity, excellent mechanical properties, and controllable surface functional groups.

Electrical conductivity

The metal atomic layer of MXenes occupies part of the lattice and has a high electron density near the Fermi level, thus maintaining high electrical conductivity[25]. The electrical conductivity of MXenes depends on the preparation method[7]. In general, large-size nanosheets and lower defect density lead to higher electrical conductivity. Conductivity ranges of MXenes from less than 1,000 S cm^{-1} to more than 10,000 S cm^{-1} can be achieved by changing the concentration of the etching agent and adding the intercalating agent[26]. The electronic properties of different MXenes vary from metallic to semiconducting. For example, MXenes containing Mo are semiconductor-like, whereas $Ti_3C_2T_x$ displays metallic characteristics[27]. Notably, regulating surface functional groups can also change the conductivity of MXenes. For example, the surface functional group of $Ti_{n+1}C_n$ modified by Te^{2-} produces an interfacial lattice expansion of about 20%

[Figure 3A]. The influence of surface functional groups on the conductivity of Ti_3C_2 MXene (TiMX) was studied using density functional theory (DFT) calculation and non-equilibrium Green's functional formalism[28]. It is found that TiMX with -F and -OH functional groups exhibited a large transmission over a wide range of electron energies, while TiMX with the -O functional group showed the smallest electron transfer. The variation of the transmission spectrum was attributed to the localization of the electronic states and the oscillation of the electrostatic potential distribution, which was largely dependent on the type of surface functional groups. It is worth noting that various surface functional groups significantly influence the electron and ion transport properties of MXenes. Nb_2C with some different functional groups [such as Nb_2CS_2, Nb_2CSe, and $Nb_2C(NH)_2$] exhibited superconductivity in the low temperature region [Figure 3B][29]. In summary, the excellent electrical conductivity of MXenes is conducive to electron transport for NO_3^-RR.

Mechanical property

The theoretical calculation (molecular dynamics and DFT) and experimental study further show that MXenes have a strong Young's modulus and thus exhibit excellent mechanical properties. A single component $Ti_3C_2T_x$ film (5 μm) can withstand 4,000 times its own weight, and further mechanical properties can be enhanced by combining with polyvinyl alcohol (PVA) (maintaining approximately 15,000 times its weight). Other MXene-based composites have also demonstrated mechanical properties of durability and compressive resistance [Figure 3C][30]. Wan *et al.* constructed an MXenes substrate [sequentially bridged MXene (SBM)] with high mechanical strength through a sequential bridging process, in which MXenes is bridged with sodium alginate (SA) by hydrogen bonding and then bridged with Ca^{2+} by ionic bonding to form a hybrid MXene-SA building block [Figure 3D][31]. The plane tensile strength and Young's modulus of SBM sheets are 14.0 GPa and 436 MPa, respectively[31]. The same research group successfully synthesized MXene thin films [sequentially densified MXene (SDM)] with excellent mechanical strength using an ordered densification strategy[32]. Specifically, small MXene sheets are inserted to fill the gaps between multiple layers of larger sheets, and then the remaining gaps are eliminated by interinterface bridging of calcium and borate ions. The SDM has high Young's modulus (72.4 GPa) and tensile strength (739 MPa) [Figure 3E and F]. In addition, Cheng *et al.* introduced one-dimensional aramid nanofibers (ANF) to construct MXene sheets with high mechanical strength through interlayer hydrogen bonding[33]. The pressure sensor with high-strength MXene sheets shows excellent self-healing properties and mechanical stability [Figure 3G and H]. More importantly, MXene-based film electrodes can improve the yield rate and synthesis efficiency of NH_3 during NO_3^-RR.

Controlled surface chemistry

It has been mentioned in the above chapter that the physicochemical properties of MXenes can be greatly changed by simply regulating the functional groups on the surface of MXenes. Interestingly, hydrophilicity and hydrophobicity can be changed by adjusting the type and proportion of surface functional groups of MXenes[34]. On the one hand, the high hydrophilicity of MXenes can enhance the solid-liquid interface between the catalysts and the electrolyte, which is conducive to promoting the diffusion of NO_3^-. On the other hand, the negatively charged MXenes can be self-assembled with other materials by electrostatic interaction, which is conducive to constructing heterostructures for high-performance NO_3^-RR. In addition, adjusting the surface functional groups can effectively enhance the interaction between MXenes and NO_3^-/N-intermediates, thus improving the catalytic performance. The surface functional groups of MXenes can form hydrogen bond interactions with water molecules. The hydrophilicity of MXenes increases through the transition from the -O and -F functional groups to the -OH functional groups[34]. As a weak hydrogen bond acceptor, the -O and -F functional groups are only slightly accessible to water. In contrast, -OH functional groups can act as hydrogen bond donors, resulting in shorter bonding distances and stronger interactions. Sun *et al.* proposed that appropriate hydrophobicity of the electrocatalyst could

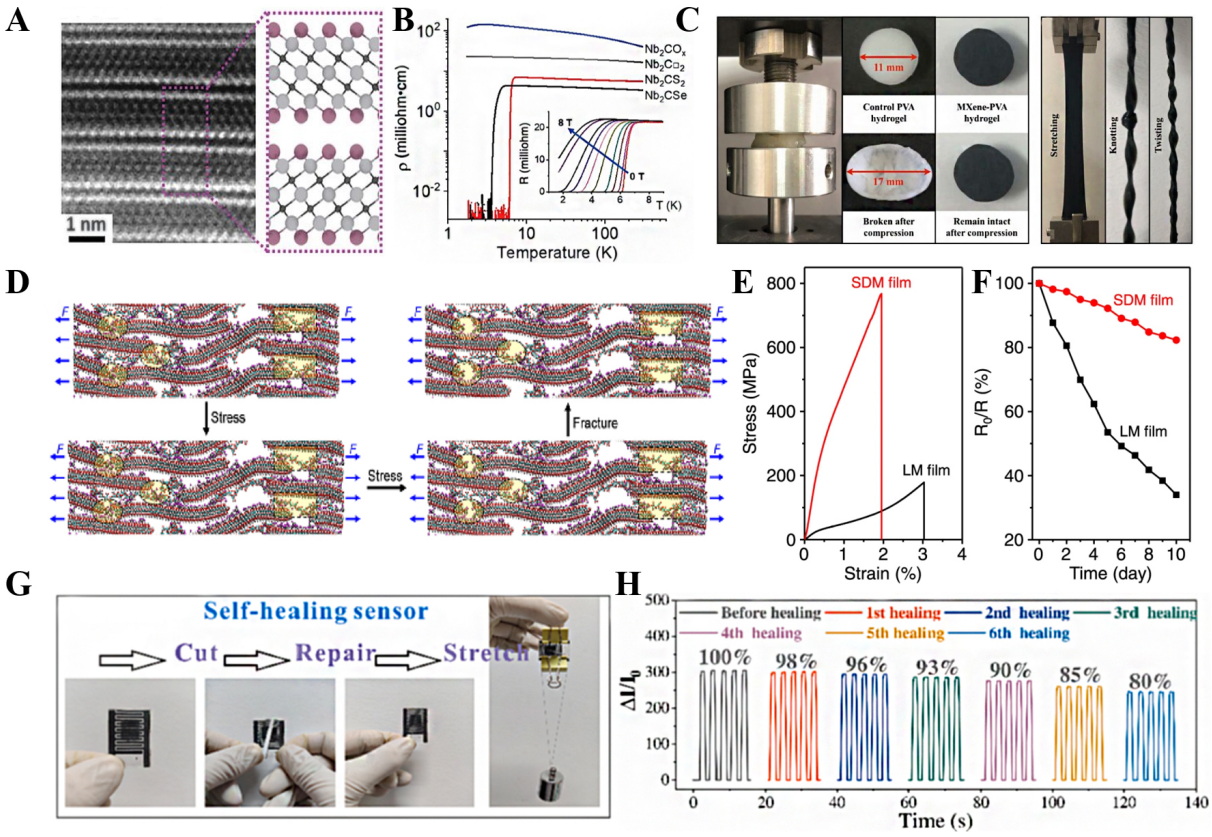

Figure 3. (A) HAADF images of Ti_3C_2Te. (B) The resistivity of Nb_2CT_n MXenes at different temperatures. (Inset) Resistance of Nb_2CS_2 MXene with temperature under different applied magnetic fields. Reproduced with permission from Ref.[29]. Copyright 2020 American Association for the Advancement of Science. (C) Optical photos of mechanical test on MXene-PVA. Reproduced with permission from Ref.[30]. Copyright 2020 Royal Society of Chemistry. (D) Schematic diagram of an SBM sheet simulating the stretching process. Reproduced with permission from Ref.[31]. Copyright 2020 National Academy of Sciences. (E) Tensile stress-strain curves of SDM films. (F) Relation between conductivity retention percentage and time of SDM films under humid conditions. Reproduced with permission from Ref.[32]. Copyright 2022 Springer Nature. (G) Self-healing process of devices made of ANF. (H) Mechanical stability of ANF in cyclic testing. Reproduced with permission from Ref[33]. Copyright 2023 Elsevier.

reduce the adsorption of H^+ and promote the diffusion of NO_3^- at the electrode interface[35]. Although the hydrophobic inner surface can reduce the reduction of H^+, a certain external environmental hydrophilicity is still required to maintain effective ion transport. Therefore, the design of MXene-based electrocatalysts with a hydrophobic inner surface and hydrophilic external surface is expected to balance the adsorption between H^+ and NO_3^-, thus improving the reaction kinetics of NO_3^-RR.

Synthesis strategy of MXenes

Until now, more than 40 MXenes have been synthesized [Figure 4A][36]. The preparation of MXenes involves various synthesis methods, which can be roughly divided into top-down and bottom-up strategies[21]. The top-down strategy refers to the synthesis of the MAX phase, and then the corresponding MXenes are obtained by selective etching of A atoms, including fluorine-containing solution etching, Lewis acid molten salt etching, electrochemical etching, and so on. In contrast, the bottom-up strategy refers to the direct synthesis of MXenes from multiple raw materials under certain conditions, including solid-state synthesis and chemical vapor deposition (CVD).

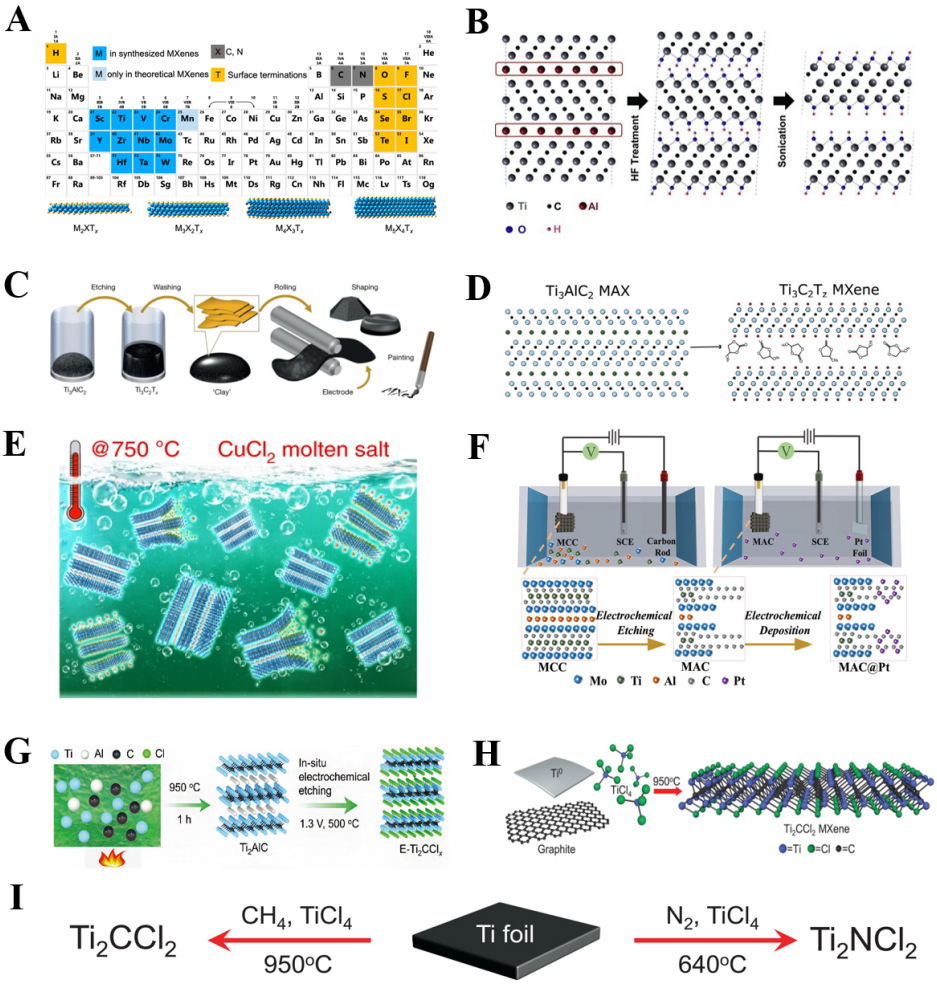

Figure 4. (A) The types of MXene that have been synthesized. Reproduced with permission from Ref.[36]. Copyright 2021 American Chemical Society. The schematic diagram of MXene is obtained by etching the MAX phase with (B) HF acid, Reproduced with permission from Ref.[18]. Copyright 2011 Wiley-VCH. (C) HCl/LiF, Reproduced with permission from Ref.[37]. Copyright 2014 Springer Nature. (D) NH_4HF_2 Reproduced with permission from Ref.[38]. Copyright 2020 Elsevier. and (E) Lewis molten salt. Reproduced with permission from Ref.[39]. Copyright 2020 Springer Nature. (F) Schematic diagram of Mo_2TiC_2 obtained by electrochemical etching of Mo_2TiAlC_2. Reproduced with permission from Ref.[41]. Copyright 2022 Wiley-VCH. (G) Schematic diagram of Ti_2CT_x obtained by electrochemical etching of Ti_2AlC. Reproduced with permission from Ref.[42]. Copyright 2023 Wiley-VCH. (H) The synthesis roadmap of MXene was obtained by solid-state method. (I) Schematic diagram of MXene synthesis by CVD. Reproduced with permission from Ref.[45]. Copyright 2023 American Association for the Advancement of Science.

Fluorine-containing solution etching method

Due to the ionic/covalent bond interaction between M-X being stronger than the metallic bond between M-A, the MAX phase can be selectively etched to remove the A-site atom to obtain the corresponding MXenes. The stripping of the A atomic layer exposes the metal elements in the M-X layer, which combines with the -F, -OH and -O in the solution to form rich surface functional groups. Naguib *et al.* successfully etched the Al layer in Ti_3AlC_2 MAX with high concentration HF to obtain $Ti_3C_2T_x$ MXene [Figure 4B][18]. However, low experimental safety and high post-processing costs limit the large-scale synthesis of MXenes using HF. Ghidiu *et al.* successfully obtained TiMX by etching Ti_3AlC_2 with *in situ* generated HF by LiF and HCl[37]. This mixture solution is safer and more effective than HF. More importantly, the multilayer MXene can be exfoliated into a few or even single layer nanosheet structure without complex post-processing [Figure 4C]. Natu *et al.* obtained MXene using HF dissociated from NH_4HF_2 in solution to etch the MAX phase [Figure 4D][38].

Lewis acid molten salt etching method

In order to get rid of the harm of fluorinated reagents, Li *et al.* developed a mild redox strategy with Lewis acid molten salts[39]. The principle is that atoms in the A layer with a lower redox potential can be oxidized by Lewis acid cations with a higher redox potential. With $CuCl_2$ as the reaction medium, Ti_3AlC_2 was dispersed in molten $CuCl_2$ at 700 °C, in which Al between Ti_3AlC_2 layers was oxidized to $AlCl_3$ and volatilized, while Cu^{2+} was reduced to Cu. Finally, TiMX was obtained by removing residual Cu after proper post-treatment [Figure 4E]. Molten salt etching proved to be a universal strategy to selectively etch numerous MAX phases (such as Si, Ga, Zn, *etc.*) and obtain the corresponding MXenes. It should be noted that reaction temperature and time are the most important factors affecting the purity of MXenes. Excessively high calcination temperatures or prolonged durations will destroy the layered structure of MXenes. Conversely, excessively low reaction temperatures or short durations will lead to incomplete MXenes etching[40]. Therefore, reasonably controlling reaction conditions is the key to obtaining high-purity MXenes using molten salt etching methods.

Electrochemical etching method

The electrochemical etching method for preparing MXenes is to selectively remove the Al atomic layer at a certain voltage using the MAX phase as the electrode. Sheng *et al.* etched Mo_2TiAlC_2 MAX by applying anode current in 0.5 M H_2SO_4 electrolyte, and high-purity Mo_2TiC_2 MXene could be obtained in a relatively short time [Figure 4F][41]. Liu *et al.* used carbon nanotubes (CNT) and reduced graphene oxide (rGO) as carbon sources to successfully prepare Ti_2AlC MAX by reacting with Ti and Al micropowders [Figure 4G][42]. Then, Ti_2CT_x MXene was obtained by *in-situ* electrochemical etching of Ti_2AlC MAX using LiCl-KCl as an electrolyte[42]. However, the matching degree of electrode voltage and the choice of electrolyte are important for electrochemical etching methods, and inappropriate matching will destroy the MAX phase.

Other etching methods

In addition to the general chemical etching methods, physical and biological approaches are also used to etch the MAX phase. Ghazaly *et al.* used surface acoustic waves (SAWs) to accelerate the conversion of Ti_3AlC_2 to $Ti_3C_2T_x$ at the millisecond level[43]. Specifically, under the promotion of ultrasonic waves (up to MHz), the protons can combine with F^- to quickly generate HF and achieve etching. Zada *et al.* used organic acids from algae to destroy V-Al bonds in the V_2AlC MAX phase and accelerate the delamination process and finally obtained V_2C MXene with higher purity[44].

Bottom-up strategy

The bottom-up strategy can omit the process of synthesizing the MAX phase, greatly saving time and cost. Current bottom-up strategies for MXene synthesis include solid-state synthesis and CVD. Solid-state synthesis is a strategy to directly synthesize MXenes by heating a mixture of precursors with a certain molar ratio at high temperatures. Wang *et al.* obtained Ti_2CCl_2 MXene by calcining the precursor mixture (graphite, Ti and $TiCl_4$) at 850 °C and obtained the maximum yield at 950 °C [Figure 4H][45]. CVD is the chemical reaction of one or more gaseous elements or compounds on the substrate surface to produce a thin film. Wang *et al.* grew MXene directly on the Ti surface by a gas mixture (Ar diluted CH_4 and $TiCl_4$ gases) at 950 °C [Figure 4I][45]. Specifically, CH_4 and $TiCl_4$ gases create a thin film on the Ti plate, and MXenes continue to grow and eventually separate from the substrate. MXenes have a unique porous microsphere morphology, which not only exposes more catalytic active sites but also increases the specific surface area[45].

RESEARCH PROGRESS OF MXENE-BASED CATALYSTS IN NO_3^-RR

Due to their unique properties, MXenes are expected to be a highly efficient electrocatalyst for NO_3^-RR. Since the electrocatalytic conversion of nitrate nitrogen to NH_3 requires nine protons coupled to eight electrons ($NO_3^- + 9H^+ + 8e^- \rightarrow NH_3 + 3H_2O$), there are multiple reaction intermediates (such as N_2, NO, NO_2 and NH_2OH, *etc.*). These intermediates further complicate the reaction mechanism of NO_3^-RR, thus posing a major challenge to achieving highly selective NH_3 synthesis. As shown in Figure 5A, the reaction pathways of NO_3^-RR can be divided into direct and indirect mechanisms[46]. For the direct mechanism, the adsorption of NO_3^- on the electrocatalysts proceeds through two pathways (electron reduction and hydrogen adsorption), initiating the electroreduction of nitrate. Subsequently, the H proton provided by water cracking combines with the N or O atom in NO_3^- without destroying the N-O bond to form NH_3. For the indirect mechanism, the dissociation process always precedes the hydrogenation process. Specifically, the N-O bond in NO_3^- is dissociated, and then a subsequent hydrogenation process is completed alone to form NH_3. As shown in Figure 5B and C, NH_3/NH_4^+ is the most thermodynamically stable form of nitrogen species at pH values of 6-9 and negative electrode potentials[47]. Although NH_3/NH_4^+ is an ideal reaction product for NO_3^-RR, different electrocatalysts can change the reaction path and product distribution of electroreduction. Since the N-O bond is difficult to break, forming $^*NO_2$ ($^*NO_3 + H_2O + 2e^- \rightarrow {}^*NO_2 + 2OH^-$) is the rate-determining step (RDS) of the whole reaction for some catalysts. Interestingly, NO_3^-RR may exhibit other RDSs on different electrocatalysts. For example, adsorption of NO_3^- ($^* + NO_3^- \rightarrow {}^*NO_3 + e^-$) becomes the RDS for CuCo alloy nanosheet[48]. In addition, the HER induced by binding two H^* is the competitive reaction of NO_3^-RR, which severely reduces the FE of NH_3 synthesis. However, the volmer step of HER can provide active hydrogen (H_{ads}) for the subsequent hydrogenation of NO_3^-. Notably, the unmodified MXene nanosheets showed modest catalytic activity for NO_3^-RR[49]. Therefore, it is valuable to design MXene-based electrocatalysts with low formation energy for H_{ads} and high formation energy for H_2 (coupling of two H_{ads}). The following chapters summarize the latest progress of MXene-based electrocatalysts in NO_3^-RR and clarify the relationship between properties and application. Table 1 summarizes the current MXene-based electrocatalysts for NO_3^-RR.

Modification of surface functional groups on MXenes

The type and proportion of surface functional groups significantly influence the electrochemical properties of MXenes[50,51]. Therefore, the rational regulation of surface functional groups is expected to improve the catalytic activity of NO_3^-RR. Cai *et al.* etched the Ti_3AlC_2 MAX phase by HCl + LiF and further exfoliated to obtain single-layer or less-layer TiMX [Figure 6A][52]. The resulting material is then annealed at low temperature in an argon atmosphere to obtain oxygen-functionalized TiMX (Of-TiMX). It is found that -O can undergo surface reconfiguration in an electrocatalytic process to form -OH, enabling it to form interfacial hydrogen bonds with NO_3^- and N-intermediates. The mechanism of -OH reaction in NO_3^- reduction is explained by detailed DFT calculation. Specifically, the H atom in -OH can combine with NO_2* to form NOOH* [Figure 6B]. The remaining O atom quickly interacts with the protons liberated by water electrolysis to form a new -OH and continues to participate in the hydrogenation process of the intermediate. It is worth noting that since the H atom preferentially adsorbs on the O atom, this effectively inhibits HER [Figure 6C]. Therefore, the feasibility of the regulation strategy of MXene surface functional groups to improve the catalytic activity of NO_3^-RR is proved both experimentally and theoretically. Of-TiMX exhibits an NH_3 yield rate of 0.99 mg h^{-1} cm^{-2} [Figure 6D]. Notably, the FE of the Of-TiMX remained above 80% in a wide voltage range and reached the maximum (90.4%) at -1.7 V [Figure 6E]. Considering the differences of active sites on the basal plane and lateral plane of MXenes, Hu *et al.* screened eight M_3C_2 MXenes (M = Ti, Mo, Nb, V, Cr, Hf, Ta, Zr) using DFT calculation and investigated their NO_3^-RR performance[53]. As shown in Figure 7A and B, NO_3^- tended to be adsorbed in the outermost layer of Ti-Ti in parallel, that is, in a 1-1 mode on the lateral plane. The RDS barrier energy of NO_3^-RR on the Ti_3C_2 basal plane ($^*NH_2 \rightarrow {}^*NH_3$, ΔG = 1.18 eV) was smaller than that on the Ti_3C_2 lateral plane ($^*NH \rightarrow {}^*NH_2$,

Table 1. Summary of MXene-based electrocatalysts for NO_3^-RR

Electrocatalysts	Electrolytes	Potential	FE	NH_3 yield	Ref.
Of-TiMX	0.5 M K_2SO_4 +200 mg L^{-1} KNO_3	-1.7 V *vs.* SCE	90.4%	0.99 mg h^{-1} cm^{-2}	[52]
CuPc@MXene	0.5 M Na_2SO_4 + 50 mg L^{-1} $NaNO_3$	-1.06 V *vs.* RHE	94%	2.72 mg h^{-1} cm^{-2}	[58]
CuBDC@$Ti_3C_2T_x$	0.1 M Na_2SO_4 + 100 mg L^{-1} $NaNO_3$	-0.7 V *vs.* RHE	86.5%	/	[62]
MIL-101(Fe)-Nb_2C	0.1 M KOH + 0.1 M KNO_3	-0.3 V *vs.* RHE	89.9%	199.68 μg h^{-1} cm^{-2}	[63]
BP/Nb_2C	0.1 M K_2SO_4 + 0.05 M KNO_3	-0.6 V *vs.* RHE	90.4%	1,967.0 μg h^{-1} cm^{-2}	[68]
$Cu_xO/Ti_3C_2T_x$	0.1 M K_2SO_4 + 0.5 M KNO_3	-0.7 V *vs.* RHE	48%	41,982 μg h^{-1} mg^{-1}	[69]
11% Bi_2O_3/MXene	0.5 M Na_2SO_4 + 1,000 mg L^{-1} KNO_3	-1.8 V *vs.* SCE	91.1%	~7.00 mg h^{-1} cm^{-2}	[71]
Ru-Cu/Cu_2O@Ti_3C_2	0.1 M KOH + 0.1 M KNO_3	-0.7 V *vs.* RHE	48.3%	199.68 μmol h^{-1} cm^{-2}	[72]
Fe_1Cu_2@MXene	0.5 M Na_2SO_4 + 100 mg L^{-1} KNO_3	-0.95 V *vs.* RHE	95.6%	90 mg after 8 h	[73]
Mo_2CT_x:Fe	0.5 M Na_2SO_4 + 100 mM $NaNO_3$	-0.6 V *vs.* RHE	70%	12.9 μmol h^{-1} $mg_{cat.}^{-1}$	[74]
FeSA/MXene	0.1 M Na_2SO_4 + 50 mg L^{-1} $NaNO_3$	-1.4 V *vs.* Ag/AgCl	82.9%	~90 μg h^{-1} cm^{-2}	[75]

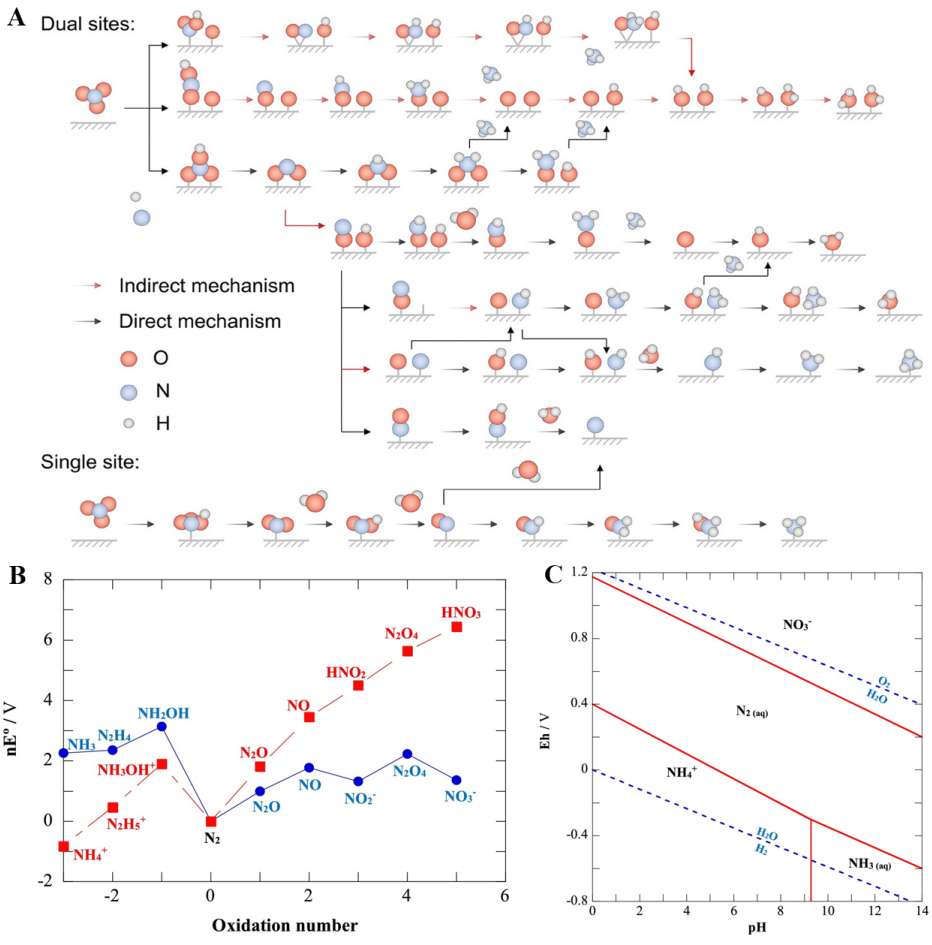

Figure 5. (A) Reaction pathways of NO_3^-RR. Reproduced with permission from Ref.[46]. Copyright 2024 Wiley-VCH. (B) Frost-Ebsworth diagrams and (C) Pourbaix diagrams of nitrogen species. Reproduced with permission from Ref.[47]. Copyright 2018 Elsevier.

ΔG = 1.69 eV), which proved that the Ti_3C_2 basal plane showed better NO_3^-RR activity [Figure 7C]. As shown in Figure 7D, the same phenomenon was found on other M_3C_2 MXenes (such as Mo_3C_2, Nb_3C_2 and V_3C_2). Notably, the reaction intermediates (such as $*NH_2$ and $*NH_3$) prone to decompose on the lateral plane of Cr_3C_2 [Figure 7E]. According to the above results, NO_3^-RR is more likely to occur on the basal plane

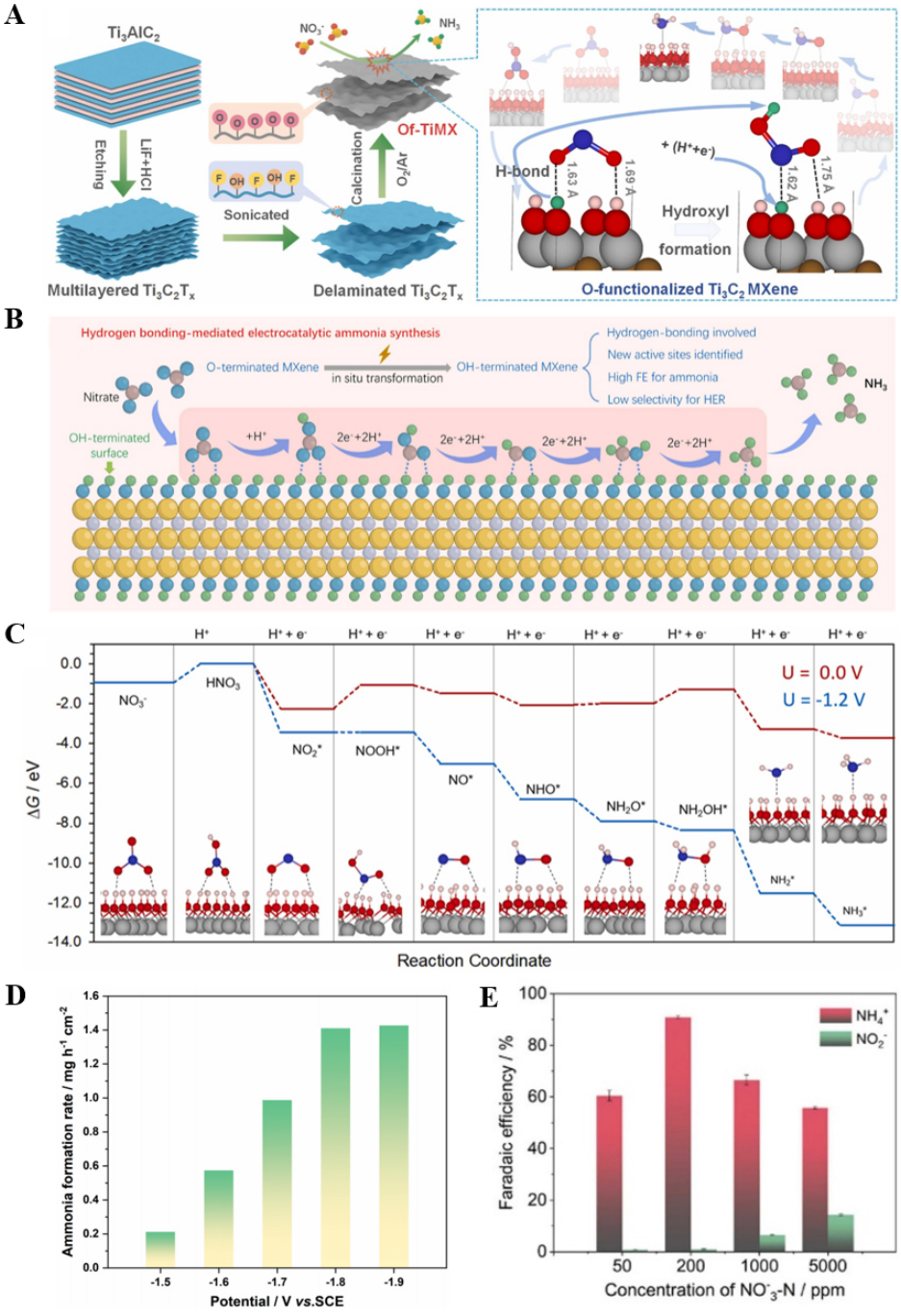

Figure 6. (A) Schematic illustration for the preparation of Of-TiMX. (B) The -O functional group is converted to the -OH of MXene. (C) Gibbs free energy barrier diagram of NO_3^-RR for Of-TiMX. (D) The NH_3 yield rate of Of-TiMX under different potentials. (E) FEs of NO_2^- and NH_4^+ for Of-TiMX at various potentials. Reproduced with permission from Ref.[52]. Copyright 2023 Elsevier.

of MXenes than on the lateral plane. In addition, it is determined that the most likely reaction path of NO_3^-RR on the MXenes basal plane is $NO_3^- \rightarrow {}^*NO_3 \rightarrow {}^*NO_2 \rightarrow {}^*NO \rightarrow {}^*N \rightarrow {}^*NH_2 \rightarrow {}^*NH_3 \rightarrow NH_3(g)$ by analyzing the thermodynamics and kinetics of the reaction intermediates. Interestingly, all unmodified M_3C_2 MXenes exhibited stronger HER and lower NO_3^-RR activity. Defect engineering (transition metal doping and functionalization) on TiMX can effectively improve the activity of NO_3^-RR. Among them, $Ti_3C_2O_2$ MXene with oxygen vacancy is considered to be the most effective NO_3^-RR electrocatalyst.

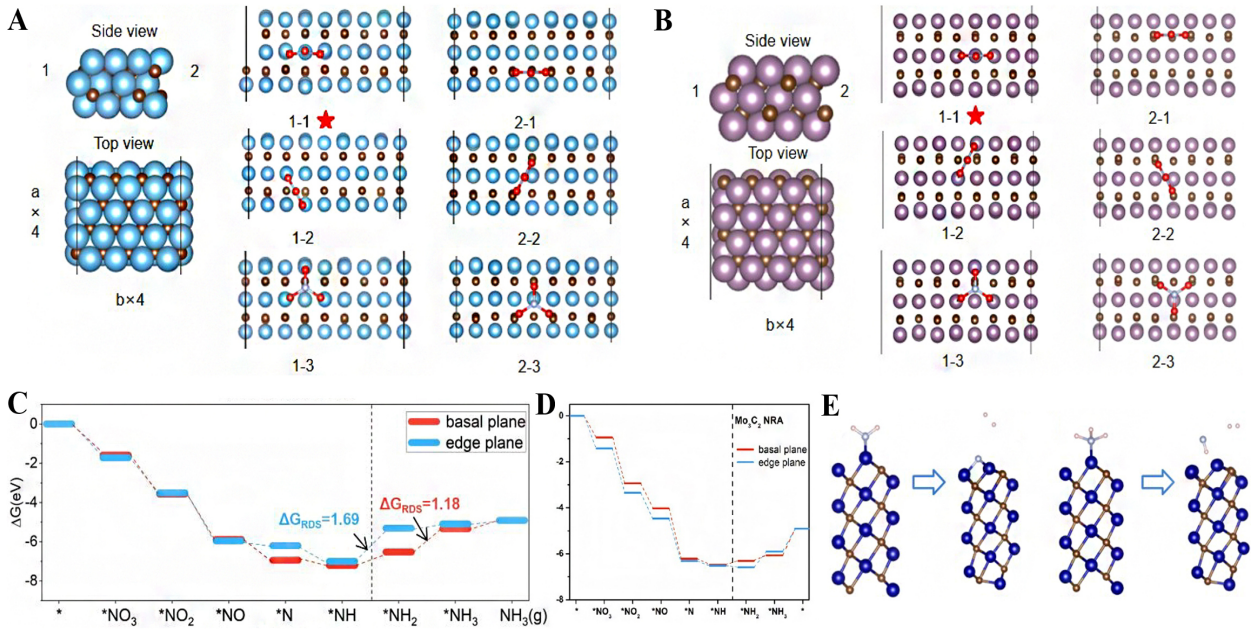

Figure 7. (A) Absorption sites on lateral plane of Ti_3C_2. (B) Absorption sites on lateral plane of Mo_3C_2. (C) Gibbs free energy diagram on basal plane and lateral plane of Ti_3C_2 during NO_3^-RR. (D) NO_3^-RR pathway on basal plane and lateral plane of Mo_3C_2. (E) Geometric configuration of $^*NH_2$ and $^*NH_3$ on Cr_3C_2 lateral plane. Reproduced with permission from Ref.[53]. Copyright 2022 Royal Society of Chemistry.

MXene-based heterostructure catalysts

Although the surface functional group regulation of MXenes can improve the electrocatalytic performance, the self-stacking and low catalytic activity of single-component MXenes have hindered their development in NO_3^-RR[54]. The heterostructure of MXenes and other materials can not only maintain the excellent properties of MXenes but also play a synergistic role of each component[55-57]. Li *et al.* used MXene-based materials for the first time to efficiently reduce NO_3^- to NH_3 by electrocatalysis[58]. Molecular copper@$Ti_3C_2T_x$ MXene (CuPc@MXene) was obtained using a simple impregnation method [Figure 8A and B]. It can be seen from the TEM images [Figure 8C] that serious agglomeration would occur when CuPc concentration was too high (20% and 40%), and uneven dispersion would occur when CuPC concentration was too low (5%). Finally, 10% CuPc@MXene was determined as the optimal catalyst. Compared with MXenes, the characteristic peaks of 10% CuPc@MXene Cu 2p and Ti 2p XPS spectra shift positively and negatively, respectively, indicating that the electron transfer between MXene and CuPc makes the heterostructure more stable [Figure 8D and E]. In addition, the electrochemical active surface area (ECSA) of 10% CuPc@MXene is two times and 2.53 times higher than that of MXene and CuPc, indicating that MXene as a carrier can greatly improve the conductivity of CuPc while dispersant CuPc to expose the abundant active sites. As shown in Figure 8F, the H_2 generation energy of CuPc is 2.17 eV, indicating that HER is effectively inhibited. Benefiting from the homogeneous dispersion of CuPc on MXene substrate and the inhibition of HER, 10% CuPc@MXene showed excellent NO_3^- conversion rate (90.5%) and NH_3 selectivity (94.0%).

Due to the self-stacking of MXenes and the poor electrical conductivity of metal-organic frames (MOF), the heterostructure of MXenes and MOF provides an effective strategy for improving electrical conductivity, structural stability and active site utilization[59-61]. Wang *et al.* synthesized 2D hybridization copper 1,4-benzenedi-carboxylate (CuBDC)@$Ti_3C_2T_x$ heterostructures through a primary growth strategy [Figure 8G][62]. It can be seen from the thermogravimetric (TG) curve that CuBDC@$Ti_3C_2T_x$ has a lower

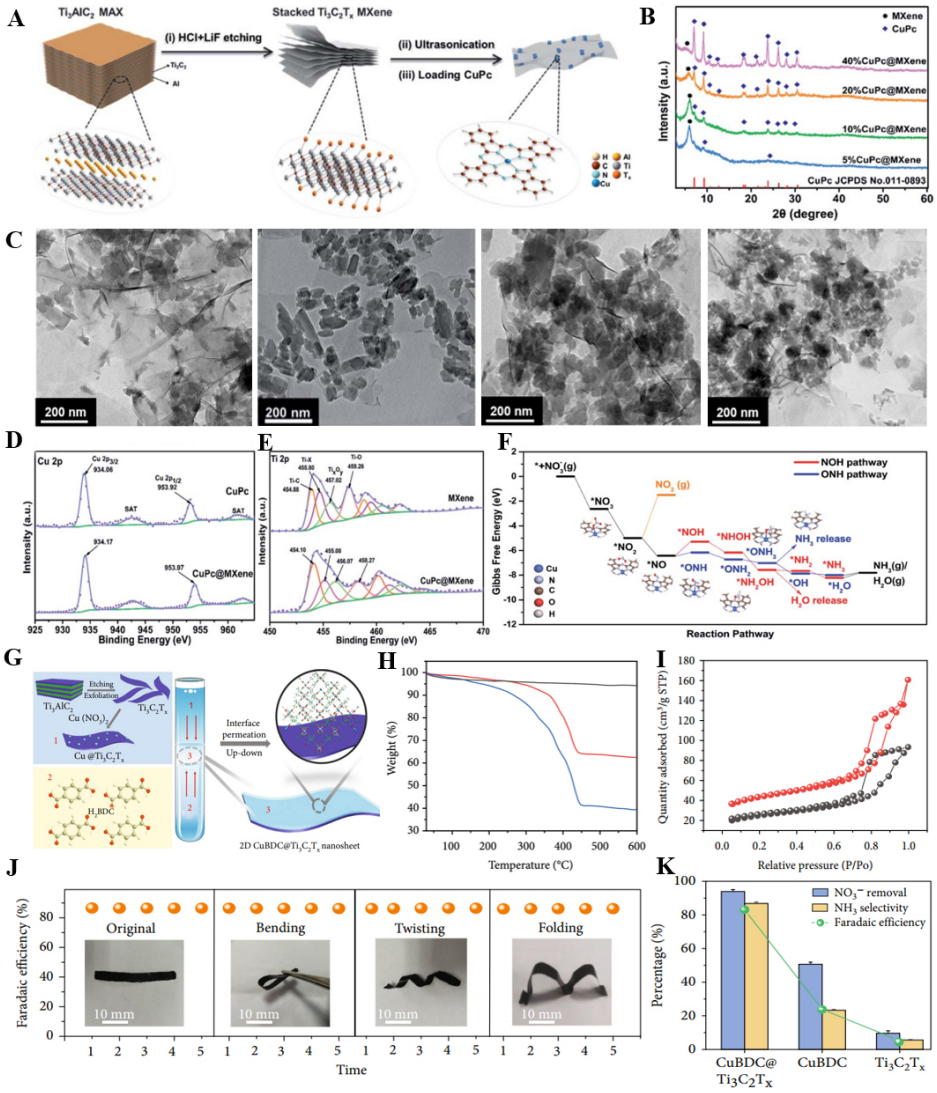

Figure 8. (A) Schematic diagram of the CuPc@MXene synthesis. (B) XRD patterns and (C) SEM images of CuPc@MXene with different proportions. High resolution XPS spectra of (D) Cu 2p and (E) Ti 2p on 10% CuPC@MXene. (F) Gibbs free energy barrier diagram of NO_3^-RR for 10% CuPc@MXene. Reproduced with permission from Ref.[58]. Copyright 2021 Royal Society of Chemistry. (G) The Synthesis route of CuBDC@$Ti_3C_2T_x$. (H) TG curves and (I) Nitrogen isothermal absorption and desorption curves of CuBDC@$Ti_3C_2T_x$. (J) Mechanical properties of CuBDC@$Ti_3C_2T_x$ film under different conditions. (K) NO_3^-RR performance of CuBDC@$Ti_3C_2T_x$. Reproduced with permission from Ref.[62]. Copyright 2022 American Association for the Advancement of Science.

weight loss rate than CuBDC, indicating that the heterogeneous structure enhances the structural stability of independent samples [Figure 8H]. CuBDC@$Ti_3C_2T_x$ has a larger specific surface area and abundant pore size distribution, which is beneficial to providing a larger solid-liquid contact area and more active sites [Figure 8I]. Interestingly, the Ti-O/Ti-C bond ration of $Ti_3C_2T_x$ (21.4%) is much higher than that of CuBDC@$Ti_3C_2T_x$ (8.2%), because the static electricity of -OH on Cu^{2+} reduces the Ti-O content. The CuBDC@$Ti_3C_2T_x$ heterostructure plays a synergistic role between CuBDC and $Ti_3C_2T_x$. As a flexible carrier, $Ti_3C_2T_x$ can not only prevent CuBDC from agglomerating but also exhibit excellent mechanical properties and structural stability [Figure 8J]. CuBDC provides a porous structure and abundant active sites, which is conducive to further improving NO_3^-RR efficiency. Thus, CuBDC@$Ti_3C_2T_x$ exhibits excellent FE (86.5%) and conversion rate (93.1%) at -0.7 V [Figure 8K]. According to the analysis of *in situ* differential

electrochemical mass spectrometry (DEMS), the reduction path of NO_3^- at CuBDC@$Ti_3C_2T_x$ is $NO_3^- \rightarrow NO_2^- \rightarrow NO \rightarrow NH_2OH \rightarrow NH_3$. In addition, Zhu *et al.* synthesized the Materials of Institut Lavoisier (MIL)-101(Fe)@Nb_2C heterostructure by a self-assembly strategy as an efficient NO_3^-RR electrocatalyst[63]. The introduction of MIL-101(Fe) gives Nb_2C more electronic states near the Fermi level, which is conducive to improving the electrical conductivity. Moreover, MIL-101(Fe)@Nb_2C shows a lower energy level gap [between the lowest unoccupied molecular orbital (LUMO) and the highest occupied molecular orbital (HUMO)], indicating a more favorable electron transfer between molecular orbitals, which proves that the construction of heterostructures is conducive to stronger chemisorption of NO_3^- and N_2. The interface of MIL-101(Fe) @Nb_2C can accelerate electron transport and improve catalytic performance through synergistic interaction. For NO_3^-RR, the FE and NH_3 yield of MIL-101(Fe)@Nb_2C reached 89.9% and 199.68 mg h^{-1} cm^{-2}, respectively. The heterogeneous structure of different 2D materials can regulate the overall electronic structure of the composite[64-67].

The heterostructure composed of MXene and other 2D materials can not only enhance the effective electron transport at the interface but also expose more active sites for efficient NO_3^-RR. Wang *et al.* synthesized black phosphorus (BP)/Nb_2C heterostructures using a simple self-assembly method[68]. The energy dispersive spectrometer (EDS) mapping shows that the elements are evenly distributed on the heterogeneous structure, which proves the successful combination of BP and MXene. The A_{1g}, B_{2g} and A_{2g} Raman peaks of BP/Nb_2C show obvious negative shift compared with BP, indicating electron transfer between Nb_2C and BP. Compared with BP nanosheets, the displacement of P $2p_{1/2}$ and P $2p_{3/2}$ peaks and the enhancement of the P-Nb bond strongly proved the existence of interfacial polarization in the heterogeneous structures. In addition, BP/Nb_2C showed higher Nb valence in X-ray Absorption Near Edge Structure (XANES) and P-Nb bond in Extended X-ray Absorption Fine Structure (EXAFS) further confirmed the results of X-ray Photoelectron Spectroscopy (XPS). From the charge density difference, it can be seen that Nb atoms mainly exist in two forms: positive Nb and BP-polarized Nb. Among them, positive Nb and BP-polarized Nb tend to bind to both sides of the N-O bond in HNO_2*, thereby synergistically promoting N-O bond cleavage to form NO*. In addition, the concentration of negative charges facilitates the stabilization of the single atom (SA) *N, facilitating the reduction of NO_3^- to NH_3. The HER kinetics of BP/Nb_2C was reflected by the Tafel curve. The Tafel slope of BP/Nb_2C (544.2 mV dec^{-1}) was higher than that of Nb_2C nanosheets (471.19 mV dec^{-1}) and BP nanosheets (321.5 mV dec^{-1}), indicating that BP/Nb_2C exhibited the lowest HER activity. Benefiting from the synergistic interaction between the two forms of Nb atoms, the FE (90.4%) and NH_3 yield (1,967 μg h^{-1} cm^{-2}) of the BP/Nb_2C heterostructure reaches maximum at -0.5 and -0.6 V, respectively.

The construction of MXenes and metal/metal oxide heterostructures can not only effectively prevent the inactivation caused by agglomeration but also realize the synergistic effect between components. Ingavale *et al.* successfully synthesized $Cu_xO/Ti_3C_2T_x$ by combustion technology[69]. During the reaction, NO_3^- escapes from $Cu(NO_3)_2 \cdot 6H_2O$ and leaves Cu^{2+} to form a Cu_xO nanofoam structure on MXenes. It is well known that the first step in NO_3^-RR is the adsorption of NO_3^- by the catalyst, but $Ti_3C_2T_x$ usually produces electrostatic repulsion on NO_3^- in solution due to the negative surface charge, which usually makes $Ti_3C_2T_x$ exhibit catalytic inertness. On the other hand, Cu_xO can better adsorb NO_3^-, but it often shows unsatisfactory catalytic activity due to poor electrical conductivity. Therefore, Cu_xO and $Ti_3C_2T_x$ composites can not only play the advantages of both but also compensate for the disadvantages of each. Regarding electrochemical properties, $Cu_xO/Ti_3C_2T_x$ exhibits a high current density (162 mA cm^{-2}), reducing energy consumption for electrocatalytic NH_3 synthesis. In terms of NO_3^-RR, $Cu_xO/Ti_3C_2T_x$ showed a high NH_3 yield (41,982 μg h^{-1} $mg_{cat.}^{-1}$) and FE (48%) at -0.7 V. In addition to MXene-based copper catalysts, bismuth has also been used in the NO_3^-RR[70]. Zhang *et al.* successfully synthesized Bi_2O_3/MXene using the hydrothermal

method [Figure 9A][71]. Bi^{3+} is first adsorbed on the MXene surface through electrostatic interaction and then converted to Bi_2O_3 in the hydrothermal process. It can be seen from X-ray diffraction (XRD) that the (002) peak in Bi_2O_3/MXene has a negative shift, indicating a strong interaction between Bi_2O_3 and MXene [Figure 9B]. Based on electrochemical impedance spectroscopy (EIS) and ECSA, Bi_2O_3/MXene showed higher electrical conductivity and exposed more active sites [Figure 9C and D]. More importantly, the Gibbs free energy shows that the proton may attack the O or N atom of *ON to form the two intermediates, ONH and NOH. Compared to the NOH pathway (1.32 eV), the energy barrier for ONH formation is only 0.42 eV. Therefore, on the surface of Bi_2O_3 (112), NO_3^- is more inclined to convert to NH_3 via the ONH pathway [Figure 9E]. For HER, the generating energy of H_2 on the surface of Bi_2O_3 (112) is far greater than the energy required to generate *NOH, which strongly proves that Bi_2O_3 can inhibit HER. The heterostructure formed by Bi_2O_3/MXene combines the inhibition effect of Bi_2O_3 on HER with the high conductivity of MXene, thus exhibiting excellent NO_3^- properties. The optimized sample (11% Bi_2O_3/MXene) exhibited 91.1% of FE and 7.00 mg h^{-1} cm^{-2} of NH_3 yield [Figure 9F].

Introducing a second metal based on a single metal site can play a tandem role in improving the activity of NO_3^-RR. Zhao *et al.* used a self-assembly strategy to form a Ru-Cu/Cu_2O@Ti_3C_2 catalyst[72]. Due to the active catalytic center of Ru, the synergistic effect between Cu^{x+}/Cu^+ and the fast electron migration rate of Ti_3C_2, Ru-Cu/Cu_2O@Ti_3C_2 showed excellent NH_3 yield (128.35 μmol cm^{-2} h^{-1}) and FE (48.3%) at -0.7 V. The synergistic effect between non-precious metals can not only show high activity to NO_3^-RR but also save the cost of catalyst synthesis. Wang *et al.* successfully prepared FeCu@MXene using a simple impregnation method[73]. The existence forms of Fe and Cu on MXene were determined by XPS, and the characteristic peaks of Fe^{3+} were observed in the Fe 2p XPS spectrum, indicating that Fe exists in the form of FeOOH. In addition, the characteristic peaks of Cu-Cl bonds in the Cl 2p and Cu 2p XPS spectra indicate that Cu exists in the form of CuCl. According to the reaction energy barrier diagram of NO_3^-RR, there is a low *NO_2 formation energy on the CuCl surface but a high *ONH (*ON hydrogenation) formation energy. Therefore, on the bimetallic Fe_1Cu_2@MXene catalyst, NO_3^- may first be adsorbed by the CuCl site and reduced to *ON and then migrate to the FeOOH site for subsequent hydrogenation. The tandem catalysis between Fe and Cu sites and the high conductivity of MXene not only effectively inhibited the competitive HER but also significantly improved the NO_3^-RR performance. Compared with Fe@MXene and Cu@MXene, the selectivities of NH_3 and NO_3^- conversion of the Fe_1Cu_2@MXene are up to 95.6% and 98%, respectively. In addition, Fe_1Cu_2@MXene shows excellent environmental stability at varying temperatures and pH values. In addition, Abbott *et al.* prepared iron-doped Mo_2CT_x MXene (Mo_2CT_x:Fe) using a top-down strategy [Figure 9G][74]. The valence states of Mo ions in Mo_2CTx:Fe under different conditions were studied by XANES. In the electrolyte without NO_3^-, the decrease of applied voltage leads to the negative shift of edge position, indicating that part of Mo^{4+} is transformed into Mo^{3+}/Mo^{2+} site. Interestingly, in the electrolyte containing NO_3^-, the application of voltage does not cause the Mo_2CTx:Fe edge position to move [Figure 9H]. These results not only prove that NO_3^-, as an oxidizing agent, can prevent the reduction of Mo^{4+} but also indicate that Mo and Fe in Mo_2CT_x:Fe are the active sites of NO_3^-RR. In addition, the change of coordination structure of Mo_2CT_x:Fe in acidic electrolyte was analyzed by EXAFS. Under applied voltage conditions, Mo_2CT_x:Fe has a lower mean $CN_{C/O}$ value than Mo_2CT_x, suggesting that partial Fe can promote the formation of surface vacancies at Mo sites in acidic media [Figure 9I]. Therefore, the presence of Fe Mo_2CT_x:Fe has a higher Mo reducibility and a higher O vacancy (O_v) than Mo_2CT_x. The Mo-V_O-Fe center formed by these vacancies and Mo/Fe is conducive to the adsorption of NO_3^-. In the neutral electrolyte, the NH_3 yield of Mo_2CT_x:Fe reached 12.9 μmol h^{-1} mg^{-1} and FE reached 70% [Figure 9J and K]. In the acidic electrolyte, Mo_2CT_x:Fe showed a higher yield (3.2 μmol h^{-1} mg^{-1}) and FE (41%) [Figure 9L and M].

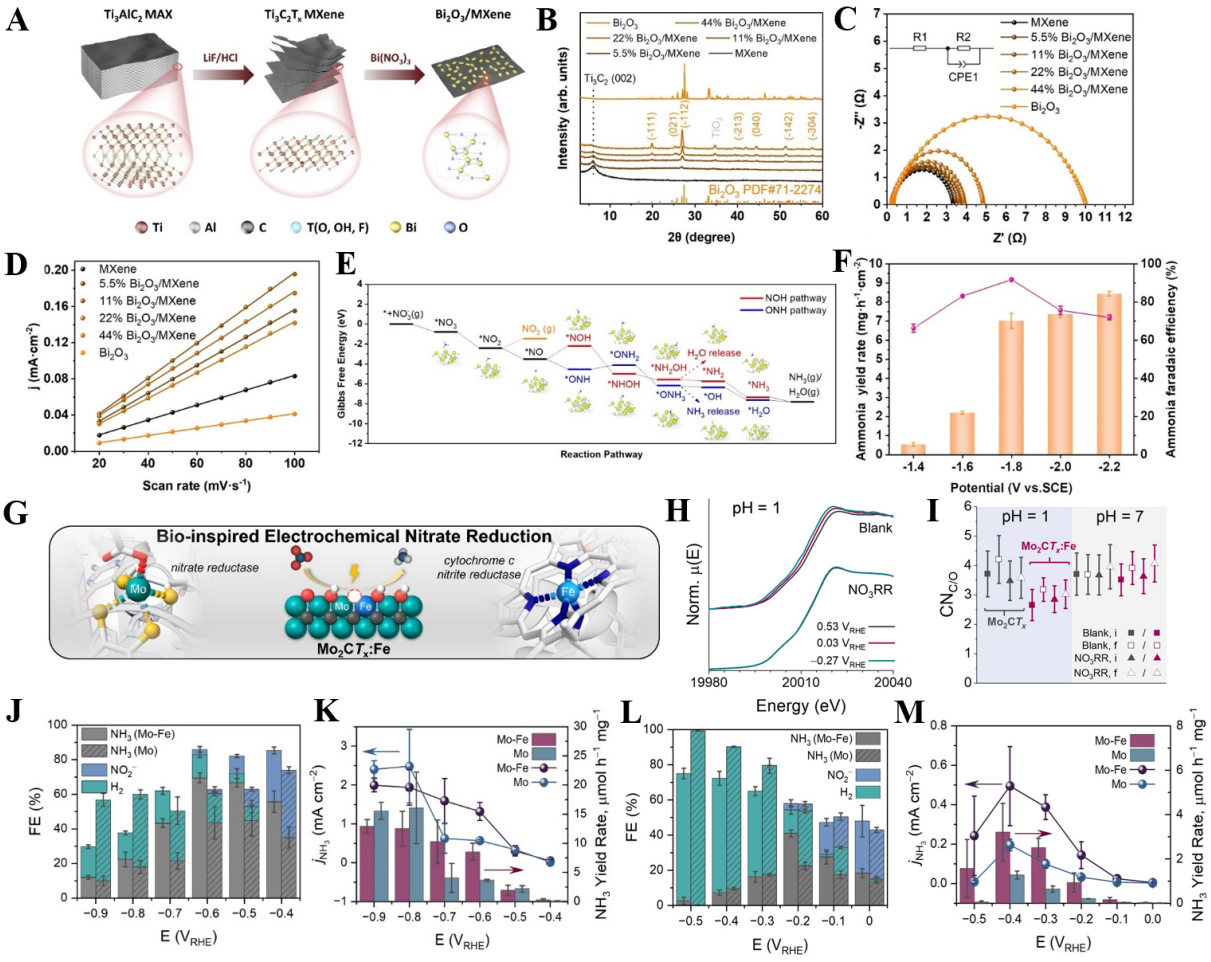

Figure 9. (A) Schematic illustration for the preparation of the Bi_2O_3/MXene. (B) XRD pattern of Bi_2O_3/MXene. (C) EIS spectra and (D) CV curves at different scan rates of Bi_2O_3/MXene with different proportions. (E) Gibbs free energy barrier diagram of NO_3^-RR for Bi_2O_3 /MXene. (F) NH_3 yield rate and FE of Bi_2O_3/MXene under different potentials. Reproduced with permission from Ref.[71]. Copyright 2023 Wiley-VCH. (G) Schematic diagram of Mo_2CT_x:Fe for NO_3^- RR. (H) XANES spectra of Mo_2CT_x:Fe in the presence or absence of NO_3^- under acidic conditions. (I) $CN_{C/O}$ was determined by FT-EXAFS data fitting for Mo_2CT_x:Fe. (J) FE of Mo_2CT_x:Fe at different potentials in neutral electrolyte. (K) Local current density and NH_3 yield rates of Mo_2CT_x:Fe at each potential in neutral electrolyte. (L) FE of Mo_2CT_x :Fe at different potentials in acid electrolyte. (M) Local current density and NH_3 yield rates of Mo_2CT_x:Fe at each potential in acid electrolyte. Reproduced with permission from Ref.[74]. Copyright 2023 Wiley-VCH.

MXene-based single atom catalysts

Recently, SA catalysts (SAC) have shown great potential in electrocatalysis due to their approximately 100% atomic utilization and well-defined active sites. Compared with other supports (carbon materials, metal oxides, polyhollow organic polymers, *etc.*), the abundant functional groups of MXene can act as the adsorption site of metal ions, which is conducive to better metal dispersion. Ren *et al.* synthesized iron SAs functionalized MXene (FeSA/MXene) using a simple impregnation method [Figure 10A][75]. In a nutshell, Fe^{3+} is spontaneously adsorbed and reduced to FeSA under the influence of abundant oxygen-containing functional groups (-O, -OH) and Ov on MXene. Through the spherical aberration corrected transmission electron microscope (AC-TEM) image of FeSA/MXene, evenly dispersed bright spots smaller than 1 nm can be observed, which strongly proves the existence of iron SAs on MXene [Figure 10B]. XPS and XANES spectra indicated that the valence of Fe is between 0 and +3 [Figure 10C and D]. EXAFS determined that Fe forms a coordination structure of Fe-O_4 [Figure 10E]. Electrochemical performance shows that large ECSA and low resistance give FeSA/MXene abundant active sites and excellent electrical conductivity. It is

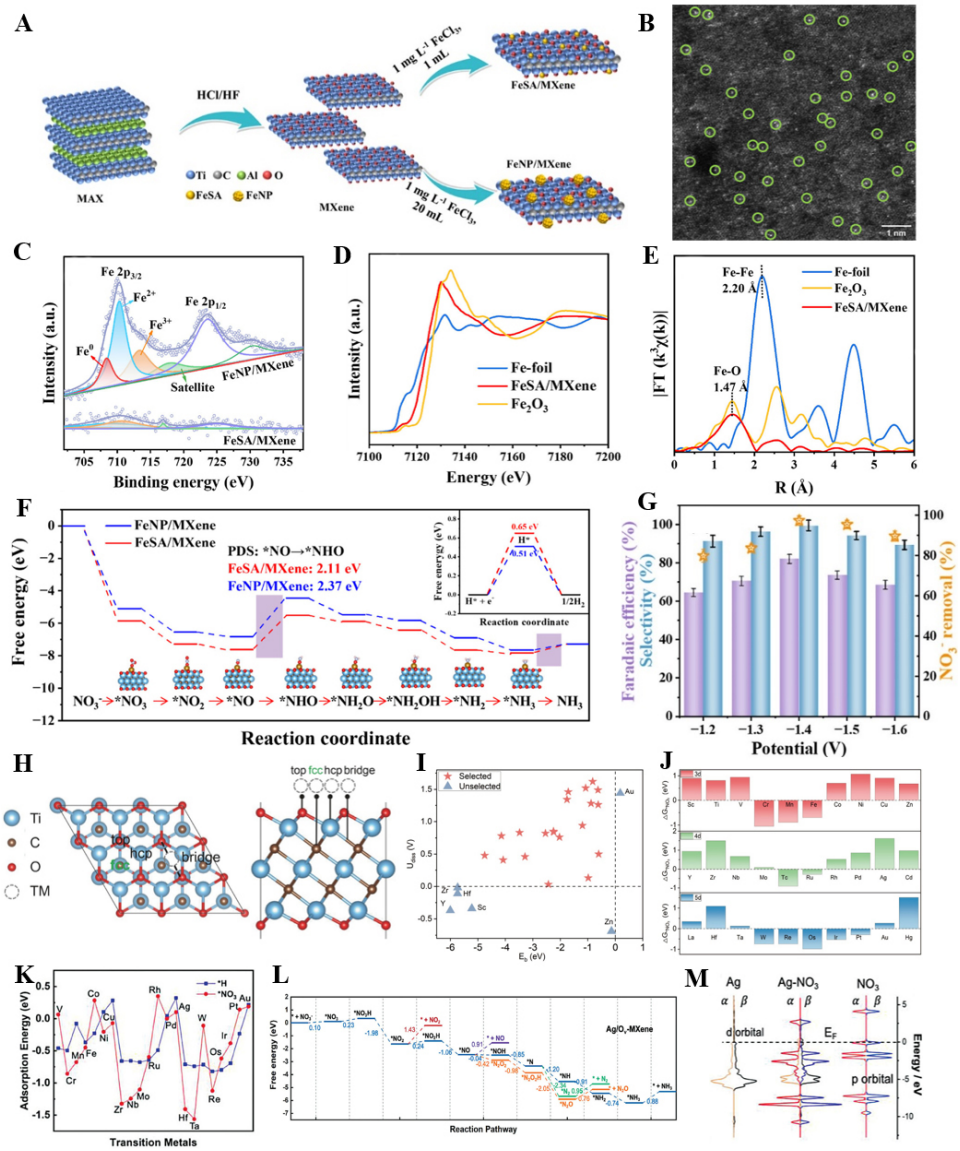

Figure 10. (A) Schematic illustration for the preparation of the FeSA/MXene. (B) AC-TEM image of FeSA/MXene. (C) High resolution XPS spectra of Fe 2p on FeSA/MXene. (D) XANES spectra of FeSA/MXene at the Fe K-edge. (E) EXAFS spectra of FeSA/MXen at the Fe K-edge. (F) Gibbs free energy barrier diagram of NO_3^-RR and (Inset) HER for Fe_1Cu_2@MXenes. (G) The NH_3 selectivity, NO_3^- removal rate and FE of FeSA/MXene under different potentials. Reproduced with permission from Ref.[75]. Copyright 2023 American Chemical Society. (H) Top view and side view of the most stable structure ($Ti_3C_2O_2$). (I) Binding energy (E_b) and dissolution potential (U_{diss}) of $Ti_3C_2O_2$-TM_{SA}. (J) Adsorption energy of $Ti_3C_2O_2$-TM_{SA} for NO_3^-. Reproduced with permission from Ref.[76]. Copyright 2023 Springer Nature. (K) Comparison of adsorption energies on TM/Ov-MXene for NO_3^- and H^+. (L) Gibbs free energy barrier diagram of NO_3^-RR Ag/Ov-MXene. (M) PDOS diagram of Ag/Ov-MXene adsorption for NO_3^-. Reproduced with permission from Ref.[77]. Copyright 2023 Wiley-VCH.

determined by DFT calculation that the potential-determining step (PDS) on FeSA/MXene and FeNP/MXene is protonation of *NO (*NHO). Compared with FeNP/MXene (+2.37 eV), the energy barrier of PDS of FeSA/MXene is only +2.11 eV, indicating that NO_3^- reduction is more likely to occur on FeSA/MXene [Figure 10F]. In addition, the H_2 generation energy on FeSA/MXene is 0.65 eV, much higher than that on FeNP/MXene (0.51 eV). Therefore, FeSA/MXene can effectively inhibit the HER and reduce the energy barrier of PDS (*NO to *NHO), which is not only conducive to the increase of FE but also accelerate the progress of NO_3^-RR. Notably, the current density associated with H_2 formation decreased

significantly in the cycle test, indicating that FeSA/MXene has a lower HER rate. Compared with FeNP/MXene (FE = 69.2%, selectivity = 81.3%) and MXene (FE = 32.8%, selectivity = 52.4%), FeSA/MXene showed satisfactory selectivity (99.2%) and FE (82.9%) [Figure 10G].

High throughput screening of MXene-based electrocatalysts can not only clarify the catalytic active site but also provide ideas and theoretical basis for experimental design. Wang *et al.* conducted first-principle calculation and screening of MXene-based electrocatalyst in NO_3^-RR from three aspects of structural stability, activity and selectivity[76]. The most stable structure ($Ti_3C_2O_2$) and the most likely reaction path [$NO_3^- \rightarrow *NO_3 \rightarrow *NO_2 \rightarrow *NO \rightarrow *N \rightarrow *NH \rightarrow *NH_2 \rightarrow *NH_3 \rightarrow NH_3$ (g)] of MXenes were determined by DFT calculation [Figure 10H]. The thermodynamic stability of TM_{SA} was evaluated by its binding energy on $Ti_3C_2O_2$. Among these 30 catalysts, only eight TMs (Sc, Zn, Y, Zr, Cd, Hf, Au, and Hg) did not meet the criteria for thermodynamic stability ($E_b < 0$ eV and $U_{diss} > 0$ V), indicating that the excellent structural stability comes from the strong TM-O [Figure 10I]. By changing reaction free energy and Fermi level, it can be analyzed that the binding energy of NO_3^- of metal atoms near d5 is higher than that of other metal atoms, because the high d-band center is conducive to stronger adsorption of N-intermediates [Figure 10J]. Finally, the competition between NO_3^-RR and HER is studied by the limit potential. $Ti_3C_2O_2$-TM_{SA} (TM = Cr, Re and O_S) are all located in the selectivity region of NO_3^-RR, which means that catalysts have higher NH_3 selectivity. Therefore, the high catalytic activity of $Ti_3C_2O_2$-TM_{SA} is attributed to the excellent structural stability, the strong interaction between TMs and NO_3^-, and the high electron density of TM_{SA} near the Fermi level. Moreover, Gao *et al.* systematically investigated the NO_3^-RR mechanism on MXene-based SACs with Ov defect[77]. Although Pt/Ov-MXene has the lowest NH_3 generation energy, HER is more likely to occur at Pt/Ov-MXene. Interestingly, Cu/Ov-MXene in non-precious metals and Ag/Ov-MXene in precious metals could exhibit higher NO_3^-RR activity while inhibiting HER [Figure 10K]. In terms of selectivity, the high formation energy barrier of the by-products (NO_2, NO, N_2O and N_2) on Ag/Ov-MXene can inhibit the side reactions and effectively improve the selectivity of NH_3 [Figure 10L]. In addition, density of states (DOS) and differential charge densities reveal the excellent conductivity of Ag/Ov-MXene and the strong interaction with NO_3^- [Figure 10M]. The adsorption energy of NO_3^- on Ag/Ov-MXene is stronger than that of H^+, which is favorable to NO_3^-RR and inhibits HER. Finally, through ab initio molecular dynamics (AIMD) simulation at 500 K, it can be found that the total energy oscillates around the initial state, indicating that Cu/Ov-MXene and Ag/Ov-MXene can maintain the structure stability under experimental conditions. To better guide the design of novel MXene-based catalysts, MXene-based heterostructure catalysts and MXene-based SACs were critically analyzed [Table 2]. MXene-based heterostructure catalysts typically have two or more distinct active components, which can increase NO_3RR activity and inhibit competitive side reactions (HER)[58]. Benefiting from the synergistic effect between different components, the MXene-based heterostructure catalysts exhibit excellent FE (MIL-101(Fe)@Nb_2C = 89.9%, BP/Nb_2C = 90.4% and Bi_2O_3/Mxene = 91.1%)[63], higher than that of MXene-based SAC (FeSA/Mxene = 82.9%)[75]. Due to the strong interaction between MXene and other component materials, MXene-based heterostructure catalysts showed better cyclic stability (BP/Nb_2C = 15 cycles and Fe_1Cu_2@Mxene = 14 cycles) than MXene-based SACs (FeSA/Mxene = 5 cycles)[68]. However, MXene-based heterostructure catalysts usually have high metal loading (> 10 wt%), which inevitably leads to waste of active sites and higher preparation costs[62]. Due to the high atom utilization and excellent intrinsic activity of MXene-based monatomic catalysts, FeSA/MXene exhibited an NH_3 selectivity of nearly 100% (99.2%)[75], higher than that of MXene-based heterostructure catalysts (CuPc@Mxene = 94% and Fe_1Cu_2@Mxene = 95.6%)[58]. Therefore, FeSA/MXene can achieve excellent performance of NO_3RR with only 1.69 wt% metal loading. In addition, MXene-based SACs have a definite coordination structure and active site, which is conducive to constructing theoretical models and exploring structure-activity relations. Compared with MXene-based heterostructure catalysts, MXene-based SACs generally have simpler theoretical model systems, suitable for high-throughput screening to provide prediction and guidance for

Table 2. Advantages and disadvantages of different MXene-based catalysts

MXene-based catalysts	Advantages	Disadvantages	Ref.
MXene-based heterostructure catalysts	(i) More catalytic active sites (ii) Synergy between components (iii) Excellent structural stability (iv) Alleviation of self-stacking and oxidation for MXenes	(i) High synthesis cost (ii) Complicated preparation process (iii) Complex theoretical model (iv) Ambiguous active sites	[58]
MXene-based single atom catalysts	(i) High atom utilization (ii) High intrinsic activity (iii) Well-defined coordination structure (iv) Low synthesis cost	(i) Easily poisoned and inactivated (ii) Poor catalytic stability (iii) Monotonous active site	[75]

experiments[76]. In the future, it is hoped that research will focus on developing technically comprehensive and efficient approaches to synthesize MXene-based catalysts with ideal structural and compositions, thereby simultaneously achieving high yield, FE and selectivity for NH_3.

METHODS FOR THE DETECTION OF AMMONIA

Although the current research has made breakthroughs and progress in NO_3^-RR, low yield and external environmental pollution lead to inaccurate quantification of NH_3. In order to solve the above problems, the NH_3 yield should be verified and repeated using two or more detection methods simultaneously. Therefore, the following chapters summarized and analyzed the advantages and disadvantages of Ultraviolet-visible (UV-Vis) spectrophotometry [Indophenol blue (IB) and Nessler's reagent methods (NR)], ion chromatography (IC), and ^{1}H nuclear magnetic resonance (NMR) methods [Table 3].

Ultraviolet-visible spectrophotometry

UV-Vis determined the absorbance of the solution at different wavelengths after color development and then obtained the NH_3 concentration by comparing with the standard curve. UV-Vis methods used for NH_3 detection usually include IB and NR techniques.

Indophenol blue method

The basic principle of the IB method is that hypochlorite can oxidize NH_3 into chloramine and phenol and then be catalyzed by sodium nitrosoferricyanide to produce blue indophenol, and finally the concentration of NH_3 can be obtained by comparing its absorbance at 655 nm with the standard curve. This approach generally uses three kinds of color developing agents (A, B and C). The configuration of A is to dissolve 5 g of sodium salicylate and 5 g of sodium citrate in 100 mL of 1M NaOH, B is a sodium hypochlorite solution with 4% effective chlorine, and C is to dissolve 1 g of sodium nitroprusside in 100 mL of ultra-pure water. The 2 mL of electrolyte was mixed with 2 mL of A, 1 mL of B and 0.2 mL of C successively, and then stood for 2 h away from light.

Nessler's reagent method

The basic principle of the NR method is that potassium iodide and mercury iodide react with NH_3 to form a reddish-brown compound, and finally, the concentration of NH_3 is obtained by comparing its absorbance at 420 nm with the standard curve. The specific operation steps are as follows: 1 mL of potassium sodium tartrate solution is added to 2 mL of electrolyte solution, and Nessler's reagent is added to the above mixed solution. After reaction for ten minutes, the concentration of NH_3 is obtained by measuring the absorbance of the corresponding wavelength[78]. Compared with IB, the NR strategy can save detection time, but it is easily interfered with external ions (Cl^-, Mg^{2+} and Ca^{2+}), resulting in inaccurate quantification.

Table 3. Advantages and disadvantages of different NH_3 detection methods

NH_3 detection methods	Advantages	Disadvantages
Indophenol blue method	Simple operation and high sensitivity	Short service life of chromogenic agent
Nessler's reagent method	Time saving and high accuracy	Easily affected by external environment
Ion Chromatography method	High selectivity and sensitivity	Not applicable to systems containing metal ions
^{1}H nuclear magnetic resonance	High accuracy and resolution	High cost

UV-Vis methods have the advantages of simple operation and low analysis cost. In addition, due to the absorption of both organic and inorganic substances in the UV-visible region, UV-Vis methods have been widely used. The following are their considerations: (i) The color developer is susceptible to external contamination during configuration, so it is necessary to maintain good sanitary conditions; (ii) Excessive NH_3 concentrations in the electrolyte shall be diluted to within the detectable range of the standard curve; (iii) For the NR method, residual chlorine in the water sample used to prepare the solution will oxidize I^- to I, resulting in abnormal color development and affecting the accuracy of the results. On the one hand, water sources can be deionized or ultra-pure. On the other hand, an appropriate amount of sodium thiosulfate can be added to remove the interference of residual chlorine; and (iv) The service life of the color developer is generally about half a month, so try to make it available to ensure the accuracy of the test.

Ion chromatography method

The principle of the IC method is to use the functional groups on the stationary phase of the ion exchange column to undergo ion exchange reaction with NH_4^+ in solution to achieve NH_3 separation. This method for determining NH_3 generally includes the steps of electrolyte pre-treatment, sample injection, separation and detection. Specifically, the electrolyte needs to be pre-treated appropriately to eliminate interference that affects the experimental results, and then under specific conditions (flow rate of 1 mL min^{-1} and mesylate solution as the eluent) the electrolyte is injected into an ion exchange column for separation by ion exchange reaction. Finally, NH_3 was quantitatively determined by a conductivity detector. IC has been widely used in water quality analysis, food safety and environmental monitoring because of its advantages of simple operation, high selectivity and sensitivity. However, due to the interference of metal ions (Na^+, K^+, Cu, *etc.*) usually present in the electrolyte and catalyst, the IC method is more suitable for metal-free or low-metal leaching catalysts and acidic electrolytes.

^{1}H nuclear magnetic resonance

The principle of ^{1}H NMR is that when the sample is irradiated by an electromagnetic wave perpendicular to the external magnetic field, the magnetic nucleus will absorb the electromagnetic wave and produce a nuclear-level transition, thus generating an electromagnetic induction resonance signal in the induction coil. The specific detection steps are as follows: take out a certain amount of electrolyte and adjust the pH value of the electrolyte to weak acidity with sulfuric acid, then add maleic acid as the internal standard in the solution, and finally add deuterium reagent to the above mixed solution for NMR detection and record the peak area ratio between NH_4^+ and $C_4H_4O_4$. The NH_3 concentration in the electrolyte is determined according to the standard curve. NMR methods show high accuracy and excellent repeatability in solutions composed of different electrolytes, but the daily operation and maintenance of NMR equipment increases the cost of NH_3 detection.

CONCLUSION AND OUTLOOK

In summary, this review discusses the structure, properties, and synthesis strategies of MXenes in detail to clarify the relationship between properties and applications. Then, the recent progress of MXene-based catalysts in NO_3^-RR was summarized and different NH_3 detection methods were analyzed. Although the

performance of the MXene-based electrocatalysts has made exciting progress in NO_3^-RR, it is still in the initial stage. Therefore, it is necessary to clarify the current challenges and future prospects for NO_3^-RR.

Reasonable design of MXene-based electrocatalyst

It is well known that the performance of NO_3^-RR is highly dependent on the properties of the electrocatalyst. Reasonable design of MXene-based materials can not only further enhance the catalytic activity but also provide a deeper understanding of the mechanism of electrochemical synthesis of NH_3. The following points are the design ideas for MXene-based electrocatalysts: (i) The heterogeneous structure of MXenes with different components is considered an effective strategy for enhancing NO_3^-RR activity[79]. On the one hand, the different energy band arrangements of various phases in the heterostructure lead to a local charge redistribution at the phase interface, which facilitates enhanced adsorption and activation of reactants. On the other hand, the built-in electric field in the heterogeneous structure will separate electrons and holes to form a space charge region, which is conducive to enhancing the transport rate of electrons and ions in the heterogeneous structure; (ii) The properties of MXenes are adjusted by introducing various transition metals with approximately equal molar ratios to improve suitability for various applications. Among them, distinct metal atoms will cause lattice distortion and local stress, which is conducive to improving the local chemical activity in the MXenes structure. In addition, the unique synergistic effect of different transition metals in the MXenes can not only improve catalytic activity but also expand the application in other fields; (iii) In order to further improve the utilization of metals or alloys, SA, double atom (DA), and SA alloy (SAA) catalysts have been developed and applied to electrocatalysis[80,81]. MXenes with surface functional groups have abundant active sites, which promote adsorption and dispersion of metal ions. Therefore, they can be combined with atomically dispersed metals by electrostatic adsorption, chemical reduction or codeposition. MXene-based SA/DA/SAA catalysts with clear active sites can better clarify the catalytic mechanism, which is conducive to deepening the understanding of NO_3^-RR. In addition, the synergistic effect of multiple atoms can further improve the performance of NH_3 synthesis; and (iv) The design and development of MXene-based catalysts is a complex process that needs to consider many factors such as active center, coordination environment and adsorption capacity. The traditional method of catalyst screening mainly involves finding the optimal catalyst through a large number of experiments, necessitating a lot of time and resources. The emergence of high-throughput screening technology provides a new solution for catalyst screening[82,83]. Specifically, high-throughput systems are used to test catalysts in a short period of time and provide detailed parameters of the reaction process[84]. By analyzing the microscopic and electronic structure of the catalyst during the reaction process, the catalytic efficiency and selectivity can be quickly determined without manual intervention, thus improving the accuracy and efficiency of catalyst screening[85].

Stability improvement strategy of MXenes

The structural stability of MXenes is mainly affected by easy oxidation and self-stacking. On the one hand, the synthesis strategy will affect the oxidation resistance of MXenes. According to the reported literature[86], adding excessive Ti and Al during the synthesis of Ti_3AlC_2 can increase the stability of the $Ti_3C_2T_x$ solution from one week to more than ten months. The improved stability of $Ti_3C_2T_x$ is attributed to the reduction of vacancies and defects on the Ti surface. Therefore, exploring synthesis strategies and mechanisms is conducive to alleviating the degradation of MXene. In addition, the oxidation resistance of MXene can also be improved by changing the storage conditions of $Ti_3C_2T_x$ (such as inert atmosphere, ultra-low temperature, and organic solvents), adding antioxidants (such as inorganic salts and ascorbic acid), and surface encapsulation of $Ti_3C_2T_x$[87-89].

Although MXenes are easily oxidized, the rational use of oxidation properties also shows great potential. MXenes can be partially or completely transformed into derivatives with more active sites through *in-situ* derivation strategies, such as partial derivation of TiMX into 1D/2D TiO_2/Ti_3C_2 heterostructures and complete derivation of V_2C MXenes into V_2O_5 nanocubes[90,91]. MXene-derivatives not only expose more active sites but also improve structural stability.

The establishment of NO_3^-RR descriptors

NO_3^-RR involves a complex proton-coupled electron transfer process, so there is an urgent need to explore high-performance electrocatalysts to improve the activity of reaction. The construction of descriptors related to the NO_3^-RR performance of electrocatalysts is conducive to the in-depth study of the structure-activity. In order to study the adsorption tendency of NO_3^- on MXene-based electrocatalysts, the relationship between charge transfer of different transition metal atoms loaded on MXene with oxygen vacancy (TM/Ov-MXene) and NO_3^- adsorption energy (ΔG_{*NO3}) was constructed[92]. The theoretical calculation and fitting results showed that the charge transfer is linear with ΔG_{*NO3}, further proving that the greater the charge transfer of TM atoms, the higher the NO_3^- adsorption energy. For example, Hf/Ov-MXene has the highest charge transfer (-2.15 e^-) and, thus, exhibits the highest adsorption energy for NO_3^- (-1.41 eV). In addition, the limiting potentials of two reaction paths on TM/Ov-MXene ($^*NO_2 + H^+ + e^- \rightarrow {}^*HNO_2$ and $^*NO_3 + H^+ + e^- \rightarrow {}^*HNO_3$) have satisfactory R^2 values (0.854 and 0.968) between ΔG_{*NO3}, indicating that ΔG_{*NO3} is a good descriptor for NO_3^-RR. Therefore, the adsorption strength of NO_3^- can be used as a descriptor for the activity and selectivity of NO_3^-RR electrocatalysts. In the future, other theoretical descriptors can be established to better guide the synthesis of novel MXene-based electrocatalysts, such as coordination number, Bader charge, and the formation energy of key intermediates[92].

Exploration of NO_3^-RR mechanism

The definition of catalyst structure and reactive site can better explore the reaction mechanism of NO_3^-RR. On the one hand, synchrotron X-ray absorption spectroscopy (XAS) (XANES and EXAFS) combined with Mossbauer spectra can be used to accurately analyze the metal valence and coordination environment[93-95]. During the reaction process, the changes of the catalyst surface and N-intermediates can be observed by *in situ* Raman and *in situ* Fourier transform infrared spectroscopy (FTIR) to determine the real active sites[96,97]. On the other hand, in addition to *in situ* electrochemical characterization, *in situ* SEM and TEM can intuitively observe the morphology changes of the electrocatalyst in the working state[98,99]. Operando XAS can be used to study the dynamic working mechanism of the catalyst in NO_3^-RR. For example, the change of the electronic structure of the catalysts during the reaction can be observed in real time by operando XAS, which is conducive to elucidating the real active site[100]. More importantly, operando XAS can also be used to explore the surface reaction mechanism of catalysts, which provides a theoretical basis for designing efficient NO_3^-RR catalysts[101].

Comprehensive utilization of energy in NO_3^-RR electrolytic system

The NO_3^-RR electrocatalytic system includes NO_3^-RR at the cathode and oxygen evolution reaction (OER) at the anode. However, the energy consumed by OER accounts for 85%-90% of the entire system and produces oxygen with low added value. In order to solve the problem of energy consumption and cost, the following two strategies are provided to improve the electrolysis process: (i) Oxidation reactions of some organic compounds exhibit lower overpotential than OER, so coupling NO_3^-RR with other anode reactions (such as glycerol and formaldehyde oxidation) can not only reduce the overall energy consumption of the electrolytic system but also obtain other organic products with high added value (glycolic acid and formic acid)[102]; (ii) Since NO_3^-RR involves a multi-electron (nine-proton coupled eight-electron) path, abundant free electrons are generated during the electrocatalysis process, which lays the foundation for driving the

electrocatalytic system to provide energy to electronic devices[103,104]. The metal-NO_3^- system is formed by combining the deposition/dissolution process of metal (Zn, Mg, Al, *etc.*) with NO_3^-RR[105]. During the charging process, the cathode participates in OER, while metal deposition occurs at the anode. In the discharge process, the positive phase is NO_3^-RR, and the negative phase is metal dissolution[106]. Therefore, the metal-NO_3^- battery is a strategy of killing three birds with one stone, which can simultaneously achieve NO_3^- reduction, NH_3 synthesis and energy supply[107]; and (iii) From the perspective of sustainable development, it is of great significance to recover renewable energy from wastewater through environmental energy technology. Although significant progress has been made in converting NO_3^- pollutant to NH_3 with higher added value through electrocatalysis, efficient and continuous recovery and conversion of NO_3^- remains challenging. Compared with electrocatalysis, microbial electrochemical technologies can simultaneously remove pollutants and obtain energy output. As an emerging wastewater treatment technology, microbial fuel cells (MFC) not only can treat NO_3^- containing wastewater but also achieve superior pollutant removal rates and electricity generation[108]. In addition, the microorganisms show satisfactory reactivity and selectivity, which is conducive to improving the NH_3 yield and FE of NO_3^-RR. Therefore, combining the advantages of electrocatalysis with those of MFC is expected to achieve efficient removal and conversion of NO_3^-.

Prospect of industrialization

The electrocatalytic synthesis of NH_3 is still in the laboratory stage at present, and the following directions are expected to facilitate the large-scale production: (i) The large-scale preparation of MXenes is important for promoting industrial applications. At present, $Ti_3C_2T_x$ has been produced in large quantities as powders (50 g per batch), colloidal suspensions (5 L per batch) and films (1 m long, 10 cm wide, 940 nm thick) through HF etching in batch reactors, which indicates that the etching method makes the large-scale preparation of MXenes possible[109,110]. However, the traditional fluorine-containing etching reagents aggravate the experimental safety and environmental pollution. Considering cost, environmental protection and safety, the molten salt etching strategy may be a practical application option. When scaling the preparation of MXenes from the laboratory stage to a larger scale, attention should be paid to controlling reaction conditions (temperature, pressure, and pH) and monitoring by-products. The appropriate reaction equipment should be designed after exploring the optimal preparation conditions of MXenes. In addition, exploring the large-scale production of other types of MXenes (such as higher-order structure and non-Ti-based MXenes) is also the future development direction; (ii) Current research has focused on the synthesis of high-performance catalysts at low current densities (< 100 mA cm^{-2}), whereas electrolytic cells for industrial applications require catalysts to operate at high current densities (ampere level)[111]. Therefore, to achieve efficient NO_3^-RR at high current density, the intrinsic catalytic activity of the catalysts and the mass transfer process should be considered. On the one hand, enhancing the intrinsic catalytic activity can accelerate the reaction kinetics of NO_3^-RR, thus increasing the reaction current density. On the other hand, promoting the mass transfer process is conducive to electron transfer and ion diffusion, thereby raising the upper limit of current density; (iii) The size of laboratory electrolytic cells (length, width and height are generally less than 0.5 m) is far from meeting the industry needs, so it is urgent to develop durable and efficient large-scale electrolytic cells to improve the NH_3 yield. Notably, most current NO_3^-RR experiments use static electrolytic cells, such as H-type electrolytic cells. In order to better meet the requirements of industrialization, it is of great significance to develop an efficient flow electrolytic cell to enhance the mass transfer process of NO_3^-RR[112]; and (iv) Combining NO_3^-RR with the stripping process can produce fertilizer directly. Specifically, the NH_3 vapor in the NO_3^-RR is separated by a stripping process. The gaseous NH_3 is introduced and dissolved into the hydrochloric acid solution, and then the solid powder of NH_4Cl is formed by rotational evaporation[111]. Furthermore, NH_3 can be used as a CO_2 absorber, not only enabling carbon capture but also producing ammonium bicarbonate (NH_4HCO_3)[113]. Directly synthesizing fertilizer (NH_4Cl and NH_4HCO_3) provides a feasible way to transform nitrate-containing wastewater into valuable NH_3 products.

DECLARATIONS

Authors' contributions

Proposed the topic of this review: Cui Z, Liu J
Performed literature survey and prepared the manuscript: Cui Z
Collectively discussed and revised the manuscript: Cui Z, Peng W, Liu J
Supervision, writing - review and editing: Li C, Liu J

Availability of data and materials

Not applicable.

Financial support and sponsorship

This study is supported by the Tianjin Education Commission Scientific Research Project (No. 2023KJ293), the Natural Science Foundation of Hebei Province (No. B2022202059), the Natural Science Foundation of Tianjin (No. 23JCQNJC00370), the China Postdoctoral Science Foundation (No. 2023M740969), the National Natural Science Foundation of China (No. U20A20153), and the Open Foundation of State Key Laboratory of Chemical Engineering (No. SKL-ChE-22B05).

Conflicts of interest

All authors declared that there are no conflicts of interest.

Ethical approval and consent to participate

Not applicable.

Consent for publication

Not applicable.

REFERENCES

1. Duan G, Chen Y, Tang Y, et al. Advances in electrocatalytic ammonia synthesis under mild conditions. *Prog Energy Comb Sci* 2020;81:100860. DOI
2. Ouyang L, Liang J, Luo Y, et al. Recent advances in electrocatalytic ammonia synthesis. *Chin J Catal* 2023;50:6-44. DOI
3. Chen A, Xia BY. Ambient dinitrogen electrocatalytic reduction for ammonia synthesis. *J Mater Chem A* 2019;7:23416-31. DOI
4. Li J, Wei F, Dong C, Wang Z, Xiu Z, Han X. Recent progress of inorganic metal-based catalysts in electrocatalytic synthesis of ammonia. *Mater Today Energy* 2021;21:100766. DOI
5. Wen X, Guan J. Recent advancement in the electrocatalytic synthesis of ammonia. *Nanoscale* 2020;12:8065-94. DOI PubMed
6. Dong C, Han X. Synthesis of Cu@NC nanocube based on Cu_2O for electrocatalytic nitrogen reduction to ammonia. *Mater Today Energy* 2022;30:101181. DOI
7. Kok SHW, Lee J, Tan L, Ong W, Chai S. Mxene - a new paradigm toward artificial nitrogen fixation for sustainable ammonia generation: synthesis, properties, and future outlook. *ACS Mate Lett* 2022;4:212-45. DOI
8. Wu T, Melander MM, Honkala K. Coadsorption of NRR and HER intermediates determines the performance of Ru-N_4 toward electrocatalytic N_2 reduction. *ACS Catal* 2022;12:2505-12. DOI
9. Ren Y, Yu C, Tan X, Huang H, Wei Q, Qiu J. Strategies to suppress hydrogen evolution for highly selective electrocatalytic nitrogen reduction: challenges and perspectives. *Energy Environ Sci* 2021;14:1176-93. DOI
10. Fu X, Zhang J, Kang Y. Recent advances and challenges of electrochemical ammonia synthesis. *Chem Catal* 2022;2:2590-613. DOI
11. Jung SP, Son S, Koo B. Reproducible polarization test methods and fair evaluation of polarization data by using interconversion factors in a single chamber cubic microbial fuel cell with a brush anode. *J Clean Prod* 2023;390:136157. DOI
12. Liang J, Li Z, Zhang L, et al. Advances in ammonia electrosynthesis from ambient nitrate/nitrite reduction. *Chem* 2023;9:1768-827. DOI

13. Zhou Y, Duan R, Li H, Zhao M, Ding C, Li C. Boosting electrocatalytic nitrate reduction to ammonia via promoting water dissociation. *ACS Catal* 2023;13:10846-54. DOI
14. Qin L, Sun F, Gong Z, et al. Electrochemical NO_3^- reduction catalyzed by atomically precise $Ag_{30}Pd_4$ bimetallic nanocluster: synergistic catalysis or tandem catalysis? *ACS Nano* 2023;17:12747-58. DOI
15. Sun W, Li L, Zhang H, He J, Lu J. A bioinspired iron-centered electrocatalyst for selective catalytic reduction of nitrate to ammonia. *ACS Sustain Chem Eng* 2022;10:5958-65. DOI
16. Shahzad F, Iqbal A, Kim H, Koo CM. 2D transition metal carbides (MXenes): applications as an electrically conducting material. *Adv Mater* 2020;32:e2002159. DOI
17. Zhang T, Chang L, Xiao X. Surface and interface regulation of MXenes: methods and properties. *Small Methods* 2023;7:e2201530. DOI
18. Naguib M, Kurtoglu M, Presser V, et al. Two-dimensional nanocrystals produced by exfoliation of Ti_3AlC_2. *Adv Mater* 2011;23:4248-53. DOI
19. Anasori B, Lukatskaya MR, Gogotsi Y. 2D metal carbides and nitrides (MXenes) for energy storage. *Nat Rev Mater* 2017;2:16098. DOI
20. Naguib M, Mochalin VN, Barsoum MW, Gogotsi Y. 25th anniversary article: MXenes: a new family of two-dimensional materials. *Adv Mater* 2014;26:992-1005. DOI PubMed
21. Lim KRG, Shekhirev M, Wyatt BC, Anasori B, Gogotsi Y, Seh ZW. Fundamentals of MXene synthesis. *Nat Synth* 2022;1:601-14. DOI
22. Ma G, Shao H, Xu J, et al. Li-ion storage properties of two-dimensional titanium-carbide synthesized via fast one-pot method in air atmosphere. *Nat Commun* 2021;12:5085. DOI PubMed PMC
23. Li L, Liu W, Jiang K, Chen D, Qu F, Shen G. In-situ annealed $Ti_3C_2T_x$ MXene based all-solid-state flexible Zn-ion hybrid micro supercapacitor array with enhanced stability. *Nanomicro Lett* 2021;13:100. DOI PubMed PMC
24. Luo Y, Chen G, Ding L, Chen X, Ding L, Wang H. Efficient electrocatalytic N_2 fixation with MXene under ambient conditions. *Joule* 2019;3:279-89. DOI
25. Jiang Q, Lei Y, Liang H, Xi K, Xia C, Alshareef HN. Review of MXene electrochemical microsupercapacitors. *Energy Stor Mater* 2020;27:78-95. DOI
26. Shin H, Eom W, Lee KH, Jeong W, Kang DJ, Han TH. Highly electroconductive and mechanically strong $Ti_3C_2T_x$ MXene fibers using a deformable MXene gel. *ACS Nano* 2021;15:3320-9. DOI
27. Zhang X, Zhang Z, Zhou Z. MXene-based materials for electrochemical energy storage. *J Energy Chem* 2018;27:73-85. DOI
28. Berdiyorov GR. Effect of surface functionalization on the electronic transport properties of Ti_3C_2 MXene. *EPL* 2015;111:67002. DOI
29. Kamysbayev V, Filatov AS, Hu H, et al. Covalent surface modifications and superconductivity of two-dimensional metal carbide MXenes. *Science* 2020;369:979-83. DOI
30. Zhang W, Ma J, Zhang W, et al. A multidimensional nanostructural design towards electrochemically stable and mechanically strong hydrogel electrodes. *Nanoscale* 2020;12:6637-43. DOI
31. Wan S, Li X, Wang Y, et al. Strong sequentially bridged MXene sheets. *Proc Natl Acad Sci USA* 2020;117:27154-61. DOI PubMed PMC
32. Zhang G, Wang L, Sa R, Xu C, Li Z, Wang L. Interconnected N-doped MXene spherical shells for highly efficient capacitive deionization. *Environ Sci Nano* 2022;9:204-13. DOI
33. Cheng Y, Xie Y, Cao H, et al. High-strength MXene sheets through interlayer hydrogen bonding for self-healing flexible pressure sensor. *Chem Eng J* 2023;453:139823. DOI
34. Malaki M, Varma RS. Wetting of MXenes and beyond. *Nanomicro Lett* 2023;15:116. DOI PubMed PMC
35. Sun F, Gao Y, Li M, et al. Molecular self-assembly in conductive covalent networks for selective nitrate electroreduction to ammonia. *J Am Chem Soc* 2023;145:21491-501. DOI
36. Gogotsi Y, Huang Q. MXenes: two-dimensional building blocks for future materials and devices. *ACS Nano* 2021;15:5775-80. DOI PubMed
37. Ghidiu M, Lukatskaya MR, Zhao MQ, Gogotsi Y, Barsoum MW. Conductive two-dimensional titanium carbide 'clay' with high volumetric capacitance. *Nature* 2014;516:78-81. DOI PubMed
38. Natu V, Pai R, Sokol M, Carey M, Kalra V, Barsoum MW. 2D $Ti_3C_2T_z$ MXene synthesized by water-free etching of Ti_3AlC_2 in polar organic solvents. *Chem* 2020;6:616-30. DOI
39. Li Y, Shao H, Lin Z, et al. A general Lewis acidic etching route for preparing MXenes with enhanced electrochemical performance in non-aqueous electrolyte. *Nat Mater* 2020;19:894-9. DOI
40. Gong S, Liu H, Zhao F, et al. Vertically aligned bismuthene nanosheets on MXene for high-performance capacitive deionization. *ACS Nano* 2023;17:4843-53. DOI
41. Sheng M, Bin X, Yang Y, Tang Y, Que W. In situ electrosynthesis of max-derived electrocatalysts for superior hydrogen evolution reaction. *Small* 2022;18:e2203471. DOI
42. Liu L, Zschiesche H, Antonietti M, et al. In situ synthesis of MXene with tunable morphology by electrochemical etching of MAX phase prepared in molten salt. *Adv Energy Mater* 2023;13:2203805. DOI
43. Ghazaly AE, Ahmed H, Rezk AR, et al. Ultrafast, one-step, salt-solution-based acoustic synthesis of Ti_3C_2 MXene. *ACS Nano*

2021;15:4287-93. DOI PubMed PMC
44. Zada S, Dai W, Kai Z, et al. Algae extraction controllable delamination of vanadium carbide nanosheets with enhanced near-infrared photothermal performance. *Angew Chem Int Ed* 2020;59:6601-6. DOI
45. Wang D, Zhou C, Filatov AS, et al. Direct synthesis and chemical vapor deposition of 2D carbide and nitride MXenes. *Science* 2023;379:1242-7. DOI
46. Zhang H, Wang H, Cao X, et al. Unveiling cutting-edge developments in electrocatalytic nitrate-to-ammonia conversion. *Adv Mater* 2024;36:e2312746. DOI
47. Garcia-segura S, Lanzarini-lopes M, Hristovski K, Westerhoff P. Electrocatalytic reduction of nitrate: fundamentals to full-scale water treatment applications. *Appl Catal B Environ* 2018;236:546-68. DOI
48. Fang JY, Zheng QZ, Lou YY, et al. Ampere-level current density ammonia electrochemical synthesis using CuCo nanosheets simulating nitrite reductase bifunctional nature. *Nat Commun* 2022;13:7899. DOI PubMed PMC
49. Wang L, Zhang H, Wang B, et al. Synthesis and electrochemical performance of $Ti_3C_2T_x$ with hydrothermal process. *Electron Mater Lett* 2016;12:702-10. DOI
50. Ding L, Wei Y, Li L, et al. MXene molecular sieving membranes for highly efficient gas separation. *Nat Commun* 2018;9:155. DOI PubMed PMC
51. Luo Y, Yang H, Ying C, et al. Plasma-activated solutions regulate surface-terminating groups enhancing pseudocapacitive $Ti_3C_2T_x$ electrode performance. *Small* 2023;3:e2305383. DOI
52. Cai J, Huang J, Cao A, et al. Interfacial hydrogen bonding-involved electrocatalytic ammonia synthesis on OH-terminated MXene. *Appl Catal B Environ* 2023;328:122473. DOI
53. Hu T, Wang M, Guo C, Li CM. Functionalized MXenes for efficient electrocatalytic nitrate reduction to ammonia. *J Mater Chem A* 2022;10:8923-31. DOI
54. Du YT, Kan X, Yang F, Gan LY, Schwingenschlögl U. MXene/graphene heterostructures as high-performance electrodes for Li-ion batteries. *ACS Appl Mater Interfaces* 2018;10:32867-73. DOI PubMed
55. Chen C, Xie X, Anasori B, et al. MoS_2-on-MXene heterostructures as highly reversible anode materials for lithium-ion batteries. *Angew Chem Int Ed* 2018;57:1846-50. DOI
56. Liu F, Jin S, Xia Q, Zhou A, Fan L. Research progress on construction and energy storage performance of MXene heterostructures. *J Energy Chem* 2021;62:220-42. DOI
57. Zhang Y, Guo R, Wen J, et al. Two-dimensional/three-dimensional hierarchical self-supporting potassium ammonium vanadate@MXene hybrid film for superior performance aqueous zinc ion batteries. *J Colloid Interface Sci* 2024;665:838-45. DOI
58. Li L, Sun W, Zhang H, et al. Highly efficient and selective nitrate electroreduction to ammonia catalyzed by molecular copper catalyst@$Ti_3C_2T_x$ MXene. *J Mater Chem A* 2021;9:21771-8. DOI
59. Zhang F, Qian Y, Jin Z, et al. Recent advances in MOFs/MXenes composites: synthesis and their electrochemical energy applications. *J Energy Stor* 2023;72:108213. DOI
60. Sharma K, Hasija V, Patial S, et al. Recent progress on MXenes and MOFs hybrids: structure, synthetic strategies and catalytic water splitting. *Int J Hydrogen Energy* 2023;48:6560-74. DOI
61. Wang Y, Song J, Wong WY. Constructing 2D sandwich-like MOF/MXene heterostructures for durable and fast aqueous zinc-ion batteries. *Angew Chem Int Ed* 2023;62:e202218343. DOI
62. Wang J, Feng T, Chen J, He JH, Fang X. Flexible 2D Cu metal: organic framework@MXene film electrode with excellent durability for highly selective electrocatalytic NH_3 synthesis. *Research* 2022;2022:9837012. DOI PubMed PMC
63. Zhu H, Xue S, Zhao F, et al. MIL-101(Fe)@Nb_2C MXene for efficient electrocatalytic ammonia production: an experimental and theoretical study. *New J Chem* 2023;47:15302-8. DOI
64. Yu X, Hu Y, Luan X, et al. Microwave-assisted construction of MXene/MOF aerogel via N-metal bonds for efficient photodegradation of vapor acetone under high humidity. *Chem Eng J* 2023;476:146878. DOI
65. Liu Y, Li L, Wen A, Cao F, Ye H. A Janus MXene/MOF separator for the all-in-one enhancement of lithium-sulfur batteries. *Energy Stor Mater* 2023;55:652-9. DOI
66. Zhai H, Liu H, Zhang Y, et al. Freestanding 1T MoS_2@MXene hybrid film with strong interfacial interaction for highly reversible zinc ions storage. *J Mater Sci Technol* 2024;188:183-90. DOI
67. Liu J, Liu Y, Xu D, et al. Hierarchical "nanoroll" like $MoS_2/Ti_3C_2T_x$ hybrid with high electrocatalytic hydrogen evolution activity. *Appl Catal B Environ* 2019;241:89-94. DOI
68. Wang S, Song C, Cai Y, et al. Interfacial polarization triggered by covalent-bonded MXene and black phosphorus for enhanced electrochemical nitrate to ammonia conversion. *Adv Energy Mater* 2023;13:2301136. DOI
69. Ingavale S, Marbaniang P, Palabathuni M, Mishra N. In situ growth of copper oxide on MXene by combustion method for electrochemical ammonia production from nitrate. *Nanoscale Adv* 2024;6:481-8. DOI PubMed PMC
70. Utomo WP, Leung MKH, Yin Z, Wu H, Ng YH. Advancement of bismuth-based materials for electrocatalytic and photo(electro)catalytic ammonia synthesis. *Adv Funct Mater* 2022;32:2106713. DOI
71. Zhang H, Li L, Sun W, He J, Xu Q, Lu J. Highly dispersed in-situ grown Bi_2O_3 nanosheets on $Ti_3C_2T_x$ MXene for selective electroreduction of nitrate to ammonia. *ChemElectroChem* 2023;10:e202201001. DOI
72. Zhao F, Li G, Hua Q, et al. Correction: a two-dimensional MXene-supported CuRu catalyst for efficient electrochemical nitrate reduction to ammonia. *Catal Sci Technol* 2023;13:6075. DOI

73. Wang Y, Rahimnejad S, Sun WJ, et al. Bimetallic Cu-Fe catalysts on MXene for synergistically electrocatalytic conversion of nitrate to ammonia. *J Colloid Interface Sci* 2023;648:595-603. DOI
74. Abbott DF, Xu YZ, Kuznetsov DA, et al. Understanding the synergy between Fe and Mo sites in the nitrate reduction reaction on a bio-inspired bimetallic MXene electrocatalyst. *Angew Chem Int Ed* 2023;62:e202313746. DOI
75. Ren Y, Tian F, Jin L, et al. Fluidic MXene electrode functionalized with iron single atoms for selective electrocatalytic nitrate transformation to ammonia. *Environ Sci Technol* 2023;57:10458-66. DOI
76. Wang M, Hu T, Wang C, et al. Screening MXene-based single-atom catalysts for selective nitrate-to-ammonia electroreduction. *Sci China Mater* 2023;66:2750-8. DOI
77. Gao X, Tse ECM. Unraveling the performance descriptors for designing single-atom catalysts on defective MXenes for exclusive nitrate-to-ammonia electrocatalytic upcycling. *Small* 2024;20:e2306311. DOI PubMed
78. Zhao Y, Wu F, Miao Y, et al. Revealing ammonia quantification minefield in photo/electrocatalysis. *Angew Chem Int Ed* 2021;60:21728-31. DOI
79. Gouveia JD, Morales-garcía Á, Viñes F, Gomes JRB, Illas F. Facile heterogeneously catalyzed nitrogen fixation by MXenes. *ACS Catal* 2020;10:5049-56. DOI
80. Xie M, Tang S, Li Z, et al. Intermetallic single-atom alloy In-Pd bimetallene for neutral electrosynthesis of ammonia from nitrate. *J Am Chem Soc* 2023;145:13957-67. DOI
81. Zhang S, Wu J, Zheng M, et al. Fe/Cu diatomic catalysts for electrochemical nitrate reduction to ammonia. *Nat Commun* 2023;14:3634. DOI PubMed PMC
82. Parey V, Abraham BM, Mir SH, Singh JK. High-throughput screening of atomic defects in MXenes for CO_2 capture, activation, and dissociation. *ACS Appl Mater Interfaces* 2021;13:35585-94. DOI PubMed
83. Shang C, He X, Li X, et al. One 3D aerogel wearable pressure sensor with ultrahigh sensitivity, wide working range, low detection limit for voice recognition and physiological signal monitoring. *Sci China Mater* 2023;66:1911-22. DOI
84. Zeng Z, Chen X, Weng K, et al. Computational screening study of double transition metal carbonitrides $M'_2M''CNO_2$-MXene as catalysts for hydrogen evolution reaction. *NPJ Comput Mater* 2021;7:80. DOI
85. Lv P, Wu D, He B, et al. An efficient screening strategy towards multifunctional catalysts for the simultaneous electroreduction of NO_3^-, NO_2^- and NO to NH_3. *J Mater Chem A* 2022;10:9707-16. DOI
86. Mathis TS, Maleski K, Goad A, et al. Modified MAX phase synthesis for environmentally stable and highly conductive Ti_3C_2 MXene. *ACS Nano* 2021;15:6420-9. DOI
87. Lee Y, Kim SJ, Kim Y, et al. Oxidation-resistant titanium carbide MXene films. *J Mater Chem A* 2020;8:573-81. DOI
88. Zhao X, Vashisth A, Prehn E, et al. Antioxidants unlock shelf-stable Ti_3C_2T (MXene) nanosheet dispersions. *Matter* 2019;1:513-26. DOI
89. Wu X, Wang Z, Yu M, Xiu L, Qiu J. Stabilizing the MXenes by carbon nanoplating for developing hierarchical nanohybrids with efficient lithium storage and hydrogen evolution capability. *Adv Mater* 2017;29:1607017. DOI
90. Liu N, Yu L, Liu B, et al. Ti_3C_2-MXene partially derived hierarchical 1D/2D TiO_2/Ti_3C_2 heterostructure electrode for high-performance capacitive deionization. *Adv Sci* 2023;10:e2204041. DOI PubMed PMC
91. Liu B, Yu L, Yu F, Ma J. In-situ formation of uniform V_2O_5 nanocuboid from V_2C MXene as electrodes for capacitive deionization with higher structural stability and ion diffusion ability. *Desalination* 2021;500:114897. DOI
92. Yang Y, Peng J, Shi Z, Zhang P, Arramel A, Li N. Unveiling the key intermediates in electrocatalytic synthesis of urea with CO_2 and N_2 coupling reactions on double transition-metal MXenes. *J Mater Chem A* 2023;11:6428-39. DOI
93. Al-Temimy A, Prenger K, Golnak R, Lounasvuori M, Naguib M, Petit T. Impact of cation intercalation on the electronic structure of $Ti_3C_2T_x$ MXenes in sulfuric acid. *ACS Appl Mater Interfaces* 2020;12:15087-94. DOI PubMed
94. Djire A, Zhang H, Reinhart BJ, Nwamba OC, Neale NR. Mechanisms of hydrogen evolution reaction in two-dimensional nitride mxenes using in situ X-ray absorption spectroelectrochemistry. *ACS Catal* 2021;11:3128-36. DOI
95. Zhao N, Yang Y, Yi D, et al. Regulating Fe-O bond in $Ti_3C_2T_x$ MXene anode for high-capacity Li-ion batteries. *Chem Eng J* 2021;422:130018. DOI
96. Thakur R, VahidMohammadi A, Moncada J, et al. Insights into the thermal and chemical stability of multilayered V_2CT_x MXene. *Nanoscale* 2019;11:10716-26. DOI
97. Shi M, Wang R, Li L, et al. Redox-active polymer integrated with MXene for ultra-stable and fast aqueous proton storage. *Adv Funct Mater* 2023;33:2209777. DOI
98. Ghassemi H, Harlow W, Mashtalir O, et al. *In situ* environmental transmission electron microscopy study of oxidation of two-dimensional Ti_3C_2 and formation of carbon-supported TiO_2. *J Mater Chem A* 2014;2:14339-43. DOI
99. Firestein KL, von Treifeldt JE, Kvashnin DG, et al. Young's modulus and tensile strength of Ti_3C_2 MXene nanosheets as revealed by in situ TEM probing, AFM nanomechanical mapping, and theoretical calculations. *Nano Lett* 2020;20:5900-8. DOI
100. Peng W, Luo M, Xu X, et al. Spontaneous atomic ruthenium doping in Mo_2CT_x MXene defects enhances electrocatalytic activity for the nitrogen reduction reaction. *Adv Energy Mater* 2020;10:2001364. DOI
101. Wang C, Chen S, Xie H, Wei S, Wu C, Song L. Atomic Sn^{4+} decorated into vanadium carbide MXene interlayers for superior lithium storage. *Adv Energy Mater* 2019;9:1802977. DOI
102. Li J, Li H, Fan K, Lee JY, Xie W, Shao M. Electrocatalytic nitrate reduction to ammonia coupled with organic oxidation. *Chem Catal* 2023;3:100638. DOI

103. Guo Y, Zhang R, Zhang S, et al. Pd doping-weakened intermediate adsorption to promote electrocatalytic nitrate reduction on TiO_2 nanoarrays for ammonia production and energy supply with zinc-nitrate batteries. *Energy Environ Sci* 2021;14:3938-44. DOI
104. Jiang H, Chen GF, Savateev O, et al. Enabled efficient ammonia synthesis and energy supply in a zinc-nitrate battery system by separating nitrate reduction process into two stages. *Angew Chem Int Ed* 2023;62:e202218717. DOI
105. Zhou J, Wen M, Huang R, et al. Regulating active hydrogen adsorbed on grain boundary defects of nano-nickel for boosting ammonia electrosynthesis from nitrate. *Energy Environ Sci* 2023;16:2611-20. DOI
106. Zhang R, Guo Y, Zhang S, et al. Efficient ammonia electrosynthesis and energy conversion through a Zn-nitrate battery by iron doping engineered nickel phosphide catalyst. *Adv Energy Mater* 2022;12:2103872. DOI
107. Cui Z, Zhao P, Wang H, et al. Molten salts etching strategy construct alloy/MXene heterostructures for efficient ammonia synthesis and energy supply via Zn-nitrite battery. *Appl Catal B Environ Energy* 2024;348:123862. DOI
108. Antonopoulou G, Bampos G, Ntaikou I, et al. The biochemical and electrochemical characteristics of a microbial fuel cell used to produce electricity from olive mill wastewater. *Energy* 2023;282:128804. DOI
109. Shuck CE, Sarycheva A, Anayee M, et al. Scalable synthesis of $Ti_3C_2T_x$ MXene. *Adv Eng Mater* 2020;22:1901241. DOI
110. Zhang J, Kong N, Uzun S, et al. MXene films: scalable manufacturing of free-standing, strong $Ti_3C_2T_x$ MXene films with outstanding conductivity. *Adv Mater* 2020;32:2070180. DOI
111. Chen FY, Wu ZY, Gupta S, et al. Efficient conversion of low-concentration nitrate sources into ammonia on a Ru-dispersed Cu nanowire electrocatalyst. *Nat Nanotechnol* 2022;17:759-67. DOI
112. Mi L, Huo Q, Cao J, et al. Achieving synchronization of electrochemical production of ammonia from nitrate and ammonia capture by constructing a “two-in-one” flow cell electrolyzer. *Adv Energy Mater* 2022;12:2202247. DOI
113. Fan K, Xie W, Li J, et al. Active hydrogen boosts electrochemical nitrate reduction to ammonia. *Nat Commun* 2022;13:7958. DOI PubMed PMC